The Astrophysical Journal, 999:210 (17pp), 2026 March 10 https://doi.org/10.3847/1538-4357/ae3d33

Exo–IPM Scattering as a Hidden Gatekeeper of Narrowband Technosignatures

Vishal Gajjar[1,2] and Grayce C. Brown[1]
[1] SETI Institute, 339 Bernardo Avenue, Suite 200, Mountain View, CA 94043, USA
[2] Department of Astronomy, University of California Berkeley, Berkeley, CA 94720, USA
Received 2025 October 1; revised 2026 January 22; accepted 2026 January 24; published 2026 March 5

Abstract

Narrowband radio technosignatures can be significantly modulated by the host star's exoplanetary interplanetary medium (Exo-IPM), where turbulence in stellar winds and coronal mass ejections (CMEs) imprint spectral broadening. We present a novel framework that maps isotropic wind properties, turbulence strength, observing frequency, and geometry to the spectral broadening of narrowband technosignatures. Anchored to what is likely the largest compilation of empirical spectral-broadening measurements from solar-system spacecraft, we validate and derive a robust radial dependence of spectral broadening from the host star. For Sun-like stars, wind speeds and turbulence strengths are constrained directly from empirical measurements, while for M-dwarfs, these properties are scaled from solar values. Applied to a simulated 1 GHz survey of the nearest 10^6 stars across orbital properties, orientation, stellar population, and Exo-IPM conditions, the survival function indicates that $\sim$70% of systems produce $>$1 Hz and $>$30% produce $>$10 Hz of broadening, disproportionately affecting M-dwarf systems, which constitute $\sim$75% of the stellar population. At 100 MHz, the effects are even more pronounced, with $>$60% of systems exhibiting $>$100 Hz of spectral broadening. Although the probability of encountering a CME during a typical technosignature observation is low ($<$3%), nearly all such encounters induce additional broadening by several orders of magnitude ($>10^3$ Hz). This redistribution of power from the expected intrinsic δ-like line into Lorentzian wings suppresses the peak signal-to-noise ratio targeted by standard narrowband pipelines, biasing sensitivity limits and plausibly contributing to the persistent "Great Silence" in narrowband radio technosignature searches over the past several decades.

Unified Astronomy Thesaurus concepts: Technosignatures (2128); Search for extraterrestrial intelligence (2127); Interplanetary medium (825)

1. Introduction

Searching for technosignatures, particularly narrowband signals ($\ll$1 Hz) at radio frequencies (G. Cocconi & P. Morrison 1959), remains one of the primary objectives for existing and upcoming radio telescopes, including SKA (A. P. V. Siemion et al. 2014), ngVLA (C. Ng et al. 2022), and FAST (L. Qian 2018). These signals are theoretically optimal due to their minimal energy requirements (V. Gajjar et al. 2021) and distinct spectral properties, making them distinguishable from natural astrophysical emissions (J. Tarter 2001). Surveys are largely concentrated near 1 GHz, though lower-frequency searches by LOFAR (O. A. Johnson et al. 2023) and Murchison Widefield Array (MWA; S. J. Tingay et al. 2016) have contributed significantly due to their larger fields of view, covering millions of stars. So far, no clear indication of any putative signals have been found from a large number of these narrowband technosignature searches (e.g., J. E. Enriquez et al. 2017; D. C. Price et al. 2020; V. Gajjar et al. 2021; O. A. Johnson et al. 2023; J.-L. Margot et al. 2023; C. Choza et al. 2024; C. Painter et al. 2025). Future planned lower-frequency telescopes, such as SKA-Low, will be able to conduct some of the deepest surveys of these narrowband signals across a significant part of the sky.

These narrowband signals typically propagate with minimal dispersion; however, spectral broadening and temporal scintillation due to turbulence in the interstellar medium (ISM) and our interplanetary medium (IPM) can significantly alter their detectability (J. M. Cordes & T. J. Lazio 1991). While ISM effects on technosignatures have been analyzed (J. M. Cordes & T. J. Lazio 1991; B. Brzycki et al. 2023, 2024), the impact of IPM-induced distortions for narrowband technosignatures remains underexplored. The solar system's IPM, shaped by stellar winds, flares, and coronal mass ejections (CMEs), exhibits electron-density irregularities that induce spectral broadening. This effect was first observed by *Mariner IV* (R. M. Goldstein et al. 1967) and by *Pioneer 6* (R. Woo et al. 1976), confirming a Kolmogorov turbulence spectrum predominantly affecting lower frequencies. Further observations using *Helios 1/2, Pioneer 10/11,* and *Viking* demonstrated that spectral broadening peaks near the Sun and decreases with a power-law dependence on angular separation from the Sun (R. Woo 1978; R. Woo & J. W. Armstrong 1979). Such broadening can expand intrinsic signal widths to hundreds of hertz, but by observing at substantial spatial separation from the Sun, such broadening effects can be contained for our Sun (A. P. V. Siemion et al. 2013).

Technosignatures originating from exoplanets or planetary systems will similarly encounter density irregularities in their respective Exo-IPMs (see Figure 1). Given that Exo-IPMs are subject to stellar activity, including stellar winds and CMEs, the resultant scattering and spectral broadening effects may significantly impact detectability. While the solar system IPM has been extensively studied, Exo-IPM effects on technosignature searches have not been systematically examined. Extrapolating from our IPM studies and based on the modeling of stellar activities around other spectral-type stars, we quantify spectral broadening of a putative narrowband signals

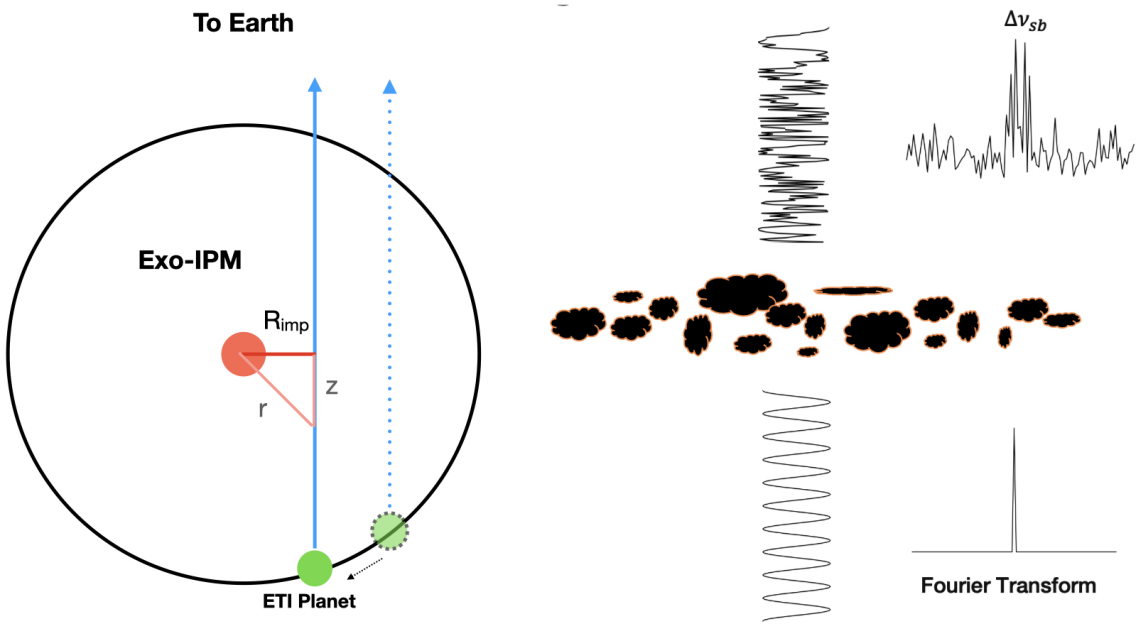

Figure 1. Left panel: schematic of an extraterrestrial transmitter on a planet (green) within the Exo-IPM, with $R_{\rm imp}$ indicating the impact distance of the passing line of sight between Earth and the ETI transmitter from the stellar object (orange). Right panel: simplified thin-screen representation of phase perturbations in a narrowband monochromatic wave propagating through a turbulent medium, showing Doppler-shifted frequencies. Temporal variations in these perturbations lead to spectral broadening of the transmitted signal.

emission across two stellar spectral types (Sun-like and M dwarfs) and all possible orbital configurations. This theoretical framework to quantify Exo-IPM-induced spectral broadening and its impact on detection strategies at GHz and sub-GHz frequencies, represents the first systematic effort to assess the Exo-IPM's role in technosignature searches. Addressing this overlooked aspect is essential to refining detection pipelines for next-generation radio technosignature searches.

Section 2 outlines the basic framework of spectral broadening and compares it with empirical evidence from the IPM. In Section 3, we provide a detailed overview of anisotropy arising from CME encounters, exploring different CME speeds and turbulence strengths. In Section 4, we provide a large sample of empirical measurements of spectral broadening that will act as an anchor in our detailed simulations. Section 5 extends these results to M dwarf stellar systems. In Section 6, we assess how the derived spectral broadening impacts a simulated technosignature survey of 10^6 stars. Finally, Section 7 summarizes the key implication of findings, and Section 8 presents our conclusions.

2. Framework

2.1. Spectral Broadening and Intensity Modulation

As a monochromatic wave front at frequency ν emitted by an extraterrestrial intelligence (ETI) transmitter propagates through the turbulent Exo-IPM (see Figure 1), stochastic electron-density fluctuations cause phase perturbations that produce scintillation and small-angle scattering. Fluctuations on large spatial scales give rise to *refractive* scintillation, which could cause centroid shifts of an ETI narrowband frequency, whereas small-scale density fluctuations produce *diffractive* scintillation, causing angular broadening and the instantaneous spectral broadening. The effect of the diffractive scintillation is more pronounced and is a cause for concern for technosignature detections; hence, we will focus on that for the remainder of this study.

As noted by B. J. Rickett (1990), a point-source wave front undergoes scattering-induced angular broadening given by

$$\theta_{\rm scattering} \approx \frac{c}{2\pi\, r_{\rm diff}\, \nu}, \tag{1}$$

where $r_{\rm diff}$ is the diffractive scale of density inhomogeneities. In a medium exhibiting Kolmogorov turbulence, the $r_{\rm diff}$ can be expressed in the units of frequency of the passing waves as $r_{\rm diff} \propto \lambda^{-6/5}\,{\rm SM}^{-3/5}$; hence, the corresponding angular broadening for an unresolved source can be expressed as

$$\theta_{\rm scattering} \propto {\rm SM}^{3/5}\, \nu^{-11/5}, \tag{2}$$

where the scattering measure (SM) is defined by

$${\rm SM} = \int_0^D C_{n_e}^2(l)\, dl. \tag{3}$$

Here, $C_{n_e}^2(l)$ represents the local strength of the turbulent fluctuations in electron density along the line of sight, and D is the distance to the source (see Figure 1 for reference). This quantity can be expressed in terms of the electron-density fluctuations $\delta n_e(l)$ and the outer scale of the turbulence $L_0(l)$ (R. Woo & J. W. Armstrong 1979; J. W. Armstrong et al. 1995) along the line of sight,

$$C_{n_e}^2(l) \propto \frac{\langle(\delta n_e(l))^2\rangle}{L_0(l)^{2/3}}. \tag{4}$$

This broadening pattern varies over time due to the transverse speed $V_\perp$ of the medium causing spectral broadening ($\Delta\nu_{\rm sb}$) via Doppler shifts (Figure 1). Following J. M. Cordes &

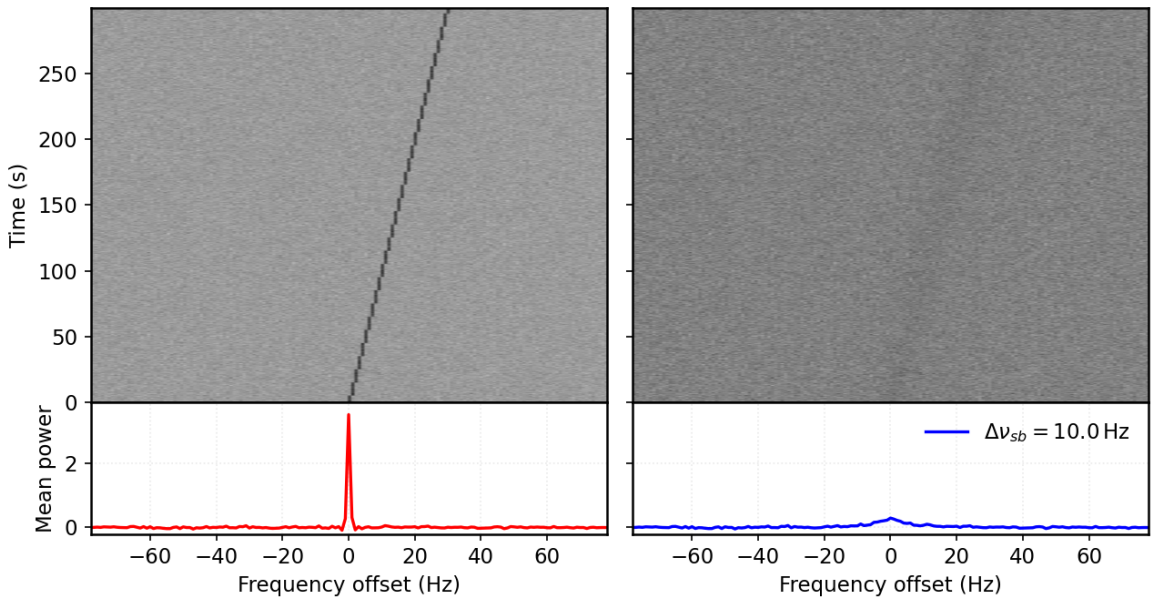

Figure 2. Left panel: simulated intrinsic narrowband signal. The top panel shows the drifting signal in a waterfall plot, while the bottom panel shows the de-drifted, time-averaged spectrum (red). Right panel: Spectrally broadened signal, where each spectrum is broadened to 10 Hz; the corresponding time-averaged spectrum is shown in blue. Due to Lorentzian broadening, signal power is redistributed into wide wings, reducing the peak signal-to-noise ratio (S/N) to 6% of the intrinsic signal's peak when broadened to 10 Hz.

T. J. Lazio (1991), we can write

$$\Delta\nu_{\rm sb} \propto \frac{V_\perp}{r_{\rm diff}} \propto V_\perp\ \nu\ \theta_{\rm scattering}. \tag{5}$$

This turbulence-driven broadening transforms an intrinsically δ-function narrowband ETI signal into a Lorentzian profile (for Kolmogorov turbulence) with width $\Delta\nu_{\rm sb}$, reducing the peak flux density (B. Brzycki et al. 2023). Figure 2 illustrates an example in which an intrinsically δ-function narrowband ETI signal is broadened by 10 Hz. Owing to the Lorentzian nature of the broadening, the energy in the line is redistributed into extended wings. For instance, if the intrinsic ETI signal is assumed to be 1 Hz wide (as is commonly adopted in radio technosignature searches), a spectral broadening of $\Delta\nu_{\rm sb}$ reduces the peak signal-to-noise ratio (S/N) by a factor of $\frac{2}{\pi}\arctan(1/\Delta\nu_{\rm sb})$. Such degradation of the intrinsic flux density not only diminishes the sensitivity of narrowband signal searches, but also hampers the performance of filter-based detection algorithms that are specifically designed to identify strictly δ-function-like signals, expecting good matching with the spectral resolution of the recorded observations (J. E. Enriquez et al. 2017; J.-L. Margot et al. 2018). It should be noted that this loss of peak power can, in principle, be recovered by a factor of $\sqrt{\Delta\nu_{\rm sb}}$ through different degrees of matched filtering. However, blind searches that do not employ matched filters will suffer significant sensitivity loss to such broadened signals.

As can be seen from Figure 1 and from Equation (5), for any line of sight extending from the ETI planet to the observer, it samples varying components of $V_\perp$ in the Exo-IPM as a function of radial distance. However, the component that contributes most significantly to the spectral broadening is likely the one that is directly perpendicular to the line of sight. In situ observations (e.g., S. Tasnim et al. 2022) have shown that beyond a few solar radii, the solar wind speed becomes nearly constant—typically around 400 km s^{-1} for the slow solar wind and up to 800 km s^{-1} for the fast wind. R. Woo (1978) also discussed the relative invariance of the solar wind speed over these scales, an assumption that greatly simplifies our model by allowing us to treat $V_\perp^{\rm max}$ as a radially constant parameter (i.e., $V_\perp \equiv V_\perp^{\rm max}$). Thus, the spectral broadening in a Kolmogorov medium may be written as a function of radial distance (r) from the star as

$$\Delta\nu_{\rm sb}(r) \propto V_\perp\ \nu^{-6/5} \left[\int_0^D C_{n_e}^2(l)\, dl\right]^{3/5}. \tag{6}$$

This same screen that causes the above-mentioned spectral broadening also sets the diffractive scintillation timescale,

$$t_{\rm diff} \sim \frac{1}{\pi\ \Delta\nu_{\rm sb}}. \tag{7}$$

J. M. Cordes & T. J. Lazio (1991) provided one of the first detailed outlines of the scintillation-induced modulation of narrowband signals in the ISM and suggested that it can help detect weak signals by enhancing its intensity by a few times while also making re-detection challenging. Recently, B. Brzycki et al. (2023) discussed extensively how this intensity modulation of the narrowband signal can be useful to discriminate between sky-localized sources with respect to radio frequency interference (RFI). The modulation experienced by the narrowband signals in the ISM environment can be applicable to the Exo-IPM environment, and it can similarly help discern between sky-localized sources with respect to RFI. Furthermore, similar to the ISM, the modulation index of this narrowband signal (m_d) imposed by this diffractive scattering from Exo-IPM can vary anywhere from $m_d << 1$ to $m_d \sim 1$, depending upon if the scattering is in the weak or strong scattering regime, respectively. We are likely to move

from the weak to the strong scattering regime as our line of sight (see Figure 1) moves closer to the star.[3] Since $t_{\rm diff}$ is directly linked to $\Delta\nu_{\rm sb}$, and prior studies (J. M. Cordes & T. J. Lazio 1991; B. Brzycki et al. 2023) have already provided extensive quantitative assessments of the $t_{\rm diff}$ impact on narrowband signals—results directly relevant to our work—we focus primarily on spectral broadening in the remainder of this paper.

2.2. Radial Dependence of $\Delta\nu_{sb}$

As defined in Equation (4), the strength of the turbulence depends on the electron-density fluctuations and the outer scale of turbulence. R. Woo (1978) highlighted that $\delta n_e(r) \propto n_e(r)$, linking density fluctuations directly to the background density profile. Solar electron-density models are most often expressed as power laws. Early models adopted offset single-term power laws, typically $\propto r^{-2}$ (e.g., E. N. Parker 1958; G. Newkirk 1967; J. Fainberg & R. G. Stone 1971; P. A. Robinson 1992; M. K. Bird et al. 1996). More recent models employ broken power laws with two or three terms, with a break occurring at or within $\sim$10 $R_\odot$, characterized by a steeper slope inside the break and a shallower slope at larger radii (e.g., K. Saito et al. 1977; Y. Leblanc et al. 1998; E. P. Kontar et al. 2019). Thus, observationally, solar wind measurements (e.g., R. Woo et al. 1976; R. Woo & J. W. Armstrong 1979; J. W. Armstrong et al. 1995; S. R. Spangler et al. 2002) demonstrate that the turbulence strength declines with the radial distance:

$$C_{n_e}^2(r) \propto r^{-q}. \tag{8}$$

From the observations of scintillation through the interplanetary medium, q approximately scales between 3 and 5 (R. Woo et al. 1976; K. Sasikumar Raja et al. 2016). S. R. Spangler & T. Sakurai (1995) used very long baseline interferometry phase-scintillation measurements of spacecraft beacons (e.g., *Helios, Pioneer*) at heliocentric distances of $\sim$5–50 $R_\odot$ to empirically determine the radial fall-off of the density-fluctuation strength. They found $q = 3.72 \pm 0.30$, consistent with a background density profile $n_e \propto r^{-2}$ and approximately constant fractional fluctuations $\delta n_e/n_e$ in the inner heliosphere. Thus, we can approximate $q \approx 4$ for our studies.

It should be noted that in Equation (6), the $C_{n_e}^2$ is integrated along the line of sight along the l-axis, while empirical measurements typically exhibit a radial dependence (r). As the main contribution on this line of sight is originating close to the star, the line-of-sight integral over l can be approximated as integral over z (see Figure 1). Thus, from Figure 1 and Equation (8), we can simplify the integral in Equation (6) as

$$\int_0^D C_{n_e}^2(l)\, dl \;\propto \int_0^D (R_{\rm imp}^2 + z^2)^{-q/2}\, dz. \tag{9}$$

Here, $R_{\rm imp}$ is the perpendicular line-of-sight impact distance from the star, and z is line-of-sight integral. The Appendix provides the solution to the integral in Equation (9), and we can write the solution as

$$\int_0^D C_{n_e}^2(l)\, dl \;\propto R_{\rm imp}^{1-q}\, \frac{\sqrt{\pi}\;\Gamma\left(\frac{q}{2} - \frac{1}{2}\right)}{2\,\Gamma\left(\frac{q}{2}\right)}. \tag{10}$$

Here, Γ is the gamma function, which can be considered a constant for a given q. It is evident that the entire integral in Equation (6) depends on the impact distance (which we will refer to as $\mathrm{R} \equiv R_{\rm imp}$) of the line of sight, as this is the location where we expect to find the largest fluctuations in electron density. Substituting $q = 4$ into Equation (10) then yields the spectral broadening law

$$\Delta\nu_{\rm sb}(R) \;\propto\; V_\perp\, \nu^{-6/5}\, R^{-9/5}. \tag{11}$$

Equation (11) shows that the radial dependence of spectral broadening follows a simple power-law form, as the turbulence strength (as defined in Equation (4)) itself has a power-law dependence on radial distance.

2.3. Latitude Dependence of $\Delta\nu_{sb}$

Observations of the solar wind indicate that the effective transverse speed $V_\perp$ varies significantly with heliographic latitude. In the solar system, fast wind—often exceeding 700–800 km s^{-1}—typically emanates from high-latitude coronal holes (A. S. Krieger et al. 1973), whereas slower wind (around 300–400 km s^{-1}) predominates near the solar equator. Consequently, a line of sight that traverses polar regions will experience a larger effective $V_\perp$, leading to greater Doppler-induced spectral broadening of a narrowband signal, while paths near the equator yield reduced broadening.

However, because $\Delta\nu_{\rm sb}$ depends on both $V_\perp$ and the turbulence strength $C_{n_e}^2$, the latitude dependence of the electron-density profile must also be considered. The dominant solar features affecting density are the polar coronal holes—which are substantially less dense than the equatorial current sheet (R. H. Munro & B. V. Jackson 1977; M. K. Bird et al. 1996; M. Guhathakurta et al. 1996). Moreover, interplanetary scintillation measurements by M. Tokumaru et al. (2000) indicate that fast coronal winds exhibit turbulence levels approximately 0.53 times those of the slower equatorial wind. Therefore, according to Equation (6), the increase in speed and the decrease in turbulence strength at high latitudes roughly cancel at the order-of-magnitude level, suggesting minimal overall latitude dependence of $\Delta\nu_{\rm sb}$. For our modeling, we thus focus solely on the radial dependence of the line of sight as the primary factor affecting $\Delta\nu_{\rm sb}$.

3. Transient Anisotropy due to CME

The Doppler-induced spectral broadening through the Exo-IPM mentioned above can additionally be modified by directional (anisotropic) electron-density fluctuations (see Figure 3), particularly during transient events such as CMEs and stellar flares. Flares induce anisotropy on smaller spatial scales and with lower bulk speeds; hereafter, we focus exclusively on CME-driven turbulence, which extends much farther out. Fast Exo-IPM CMEs—via their shock-sheath regions—inject strongly turbulent, magnetically structured plasma. Figure 3 illustrates the simplified conical CME model adopted here, an approximation advocated by H. Xie et al. (2004) and widely used in simulations (R. M. Dewey et al. 2015; L. Rodriguez et al. 2024).

[3] It is beyond the scope of our current work to estimate exact transition boundary from weak to strong scattering for an ETI transmitter operating at a certain frequency.

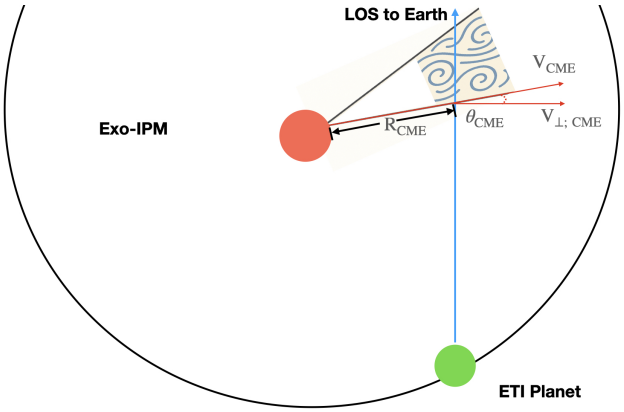

Figure 3. Simplified schematic of a CME-driven turbulent beam (shaded cone with internal turbulence) erupting from the host star (orange) and crossing the Exo-IPM. The blue arrow marks the observer's line of sight (LOS), which intersects the CME shock-sheath at impact distance R_{CME}. The ETI transmitter (green) lies on its planetary orbit. This conical CME model is adopted from H. Xie et al. (2004).

For our estimates, we can model an Exo-IPM CME as a transient "bump" of stellar-wind plasma with modified parameters, CME speed ($V_{\perp;\,CME}$), and strength of turbulence of the CME ($C^2_{n_e;\,CME}$) in Equations (4) and (6). Thus, we model the additional broadening from a transient CME crossing our line of sight as

$$\Delta\nu_{sb}(R,\,t) = \Delta\nu_{sb,iso}(R)\mathcal{B}_{ani}(R,\,t)\,, \tag{12}$$

where $\Delta\nu_{sb,iso}$ is the isotropic spectral broadening due to the ambient Exo-IPM defined earlier in Equation (6), and $\mathcal{B}_{ani}$ is the time-dependent Exo-IPM CME-induced excess "bump" broadening. In quiescent conditions, $\mathcal{B}_{ani} \approx 1$. During the CME-sheath passage, $\mathcal{B}_{ani} \gg 1$, producing the extra spectral broadening. There have been several studies to map the impact of passing this CME sheath on the IPM. For example, R. A. Fallows et al. (2023) used the LOFAR telescope to track an ultra-fast CME over 30 hr by observing a number of point sources at multiple solar impact distances ranging from 50°–82°. They reported that the IPM scintillation index jumped sharply (due to a density spike), but the wind speed and scintillation remained elevated for >7 hr after the CME front passed. Thus, the passing of a CME in the Exo-IPM across the line of sight toward any potential technosignature source is a significant event lasting for significant fraction of the period and needs to quantified. Below, we examined radial dependence of both $V_{\perp;\,CME}$ and $C^2_{n_e;\,CME}$ to access radial dependence of the anisotropy parameter $\mathcal{B}_{ani}(R)$.

3.1. Exo-IPM CME speeds

V_{CME} exhibits a wide range of values: near the stellar base, CMEs can launch at speeds from below 100 km s^{-1} up to 2600 km s^{-1} (S. Yashiro et al. 2004). Once ejected, a CME will accelerate if $V_{CME} < V_{iso}$ or decelerate if $V_{CME} > V_{iso}$ until it matches the ambient interplanetary medium speed V_{iso} (N. Gopalswamy et al. 2000; B. Vršnak et al. 2004; P. K. Manoharan 2006). As illustrated in Figure 3, our line of sight may intersect the CME shell at any radial distance (R_{CME}) from the Sun—depending on the observation time and CME geometry—so it is essential to characterize the radial evolution of V_{CME} to estimate $V_{\perp,\,CME}(R_{CME})$.

Following the aerodynamic drag-based model (B. Vršnak et al. 2004; B. Vršnak & T. Žic 2007), we use a linear-drag parameterization[4] in which the speed difference decays exponentially with a characteristic length, so we can write,

$$V_{CME}(R) = V_{iso} + (V^0_{CME} - V_{iso}) \times \exp\left[-\frac{R - R_0}{L_{drag}}\right], \tag{13}$$

where V^0_{CME} is the CME speed at $R = R_0$, V_{iso} is the local isotropic ambient-wind speed, and L_{drag} is the e-folding drag length (i.e., the excess $\Delta V = V_{CME} - V_{iso}$ decays by e over L_{drag}). For reference, empirical drag-based fits for solar CMEs imply characteristic drag lengths $L_{drag} \sim 0.2$–2 au when expressed in terms of the quadratic drag parameter reported by B. Vršnak & N. Gopalswamy (2002). More recently, J. Čalogović et al. (2025) found optimal drag parameters corresponding to $L_{drag} \sim 0.3$–0.5 au for typical CME speeds. We have adapted 0.5 au as L_{drag} for our studies.

S. Yashiro et al. (2004) and D. F. Webb & T. A. Howard (2012) compiled extensive surveys of solar CMEs over a full activity cycle, confirming that eruptions occur at all solar latitudes and span angular width Ω_{CME} of 20°–120°. A substantial fraction of these events launch at speeds exceeding 1000 km s^{-1}, with maxima up to 2600 km s^{-1} (S. Yashiro et al. 2004). Furthermore, the distribution of the speed ratio $f = V^0_{CME}/V_{iso}$ can be approximated by a chi-squared-like function spanning $f \approx 0.5$–6 (S. Yashiro et al. 2004; D. F. Webb & T. A. Howard 2012). Adopting the drag-based prescription in Equation (13), the transverse component of the CME propagation speed at distance R_{CME} can be written as

$$V_{\perp,\,CME}(R_{CME}) = V_{iso}\left[1 + (f-1) \times \exp\left(-\frac{R_{CME} - R_\odot}{L_{drag}}\right)\right] \times \cos\theta_{CME} \tag{14}$$

where $f = V^0_{CME}/V_{iso}$ is the initial speed ratio, and θ_{CME} is the angle between the CME propagation direction and the perpendicular direction to the line of sight (see Figure 3).

3.2. Exo-IPM CME Turbulence

In Sun-like stars, it is well established that CME turbulence follows a Kolmogorov-type spectrum (K. Hamilton et al. 2008), a result recently confirmed by *Wind* spacecraft observations at 1 au (Z. I. Shaikh 2024) and shown to hold across heliocentric distances (S. W. Good et al. 2023). R. A. Fallows et al. (2023) and L. Sorriso-Valvo et al. (2021) extensively discussed post-CME turbulence in the IPM at a substantial distance from the Sun. P. K. Manoharan (2010) quantified the excess turbulence due to CMEs as the `g-value`, which is a ratio between the modulation index of intensity scintillation for a source under observed conditions with respect to the averaged background conditions. The g-value during the CME is expected to increase by several factors, which can directly point toward enhanced $C^2_{n_e}$ where

[4] B. Vršnak et al. (2004) discussed a quadratic drag prescription as γ for CME kinematics; here we simplify this to a linear form for analytical convenience.

the relationship can be given as:

$$g^2 = \frac{m^2_{\rm CME}}{m^2_{\rm iso}} \approx \frac{\int C^2_{n_e,\rm CME}(z)\,dz}{\int C^2_{n_e,\rm iso}(z)\,dz}. \quad (15)$$

Here, $\int C^2_{n_e,\rm iso}(z)\,dz$ and $\int C^2_{n_e,\rm CME}(z)\,dz$ are the same integrals mentioned in Equation (6) but without and with a CME encounter, respectively. This implies that a higher g-value directly reflects increased integrated turbulence strength along the line of sight due to the CME structure. R. A. Fallows et al. (2023) reported g-values associated with a CME event observed using LOFAR, where the maximum g-value reached approximately 3 at 1 au. This corresponds to a g^2-value of around 10 in Equation (15), indicating that the integrated turbulence strength $\int C^2_{n_e;\rm CME}(z)\,dz$ during the CME was an order of magnitude higher than that in the ambient quiet solar wind.

There are no direct radial dependency measurements of the $C^2_{n_e;\rm CME}$ for solar CMEs. Thus, we will take a simple self-similar cone expansion approximation where the mean density falls as r^{-2} and the outer scale grows as r; one then finds $C^2_{n_e} \propto \delta n_e^2/L_0^{2/3} \propto r^{-4}/r^{2/3} = r^{-14/3} \approx r^{-4.67}$, i.e., a slightly steeper decline than the canonical r^{-4} of the quiescent Exo-IPM (see Section 2.2). Plugging this into Equation (6), we can approximate it as

$$C^2_{n_e;\,\rm CME}(R_{\rm CME}) \approx 10\left(\frac{R_{\rm CME}}{215\,R_\odot}\right)^{-0.67} C^2_{n_e;\,iso}(R_{\rm CME}). \quad (16)$$

This approximation is also supported by some indirect measurements. For example, S. W. Good et al. (2023) tracked one CME sheath from 0.47 au to 1.08 au and, assuming that magnetic fluctuations also follow density fluctuations ($\delta B \sim \delta n_e$), they reported a steeper decline in the turbulence during the CME compared to regular solar wind. Similarly, L. Sorriso-Valvo et al. (2021) conducted a detailed analysis of turbulence properties before, during, and after a CME event observed by the *Wind* spacecraft. They found that the turbulent energy transfer rate within the CME sheath was significantly higher than in the ambient solar wind but decreased more rapidly with distance. This suggests that the enhanced turbulence generated by the CME shock dissipates faster radially than the background solar wind turbulence.

3.3. Defining $\mathcal{B}_{\rm ani}(R, t)$

Combining these observational signatures and Equations (13) and (16), we can approximate the spectral broadening "bump" due to anisotropy introduced by CMEs as

$$\mathcal{B}_{\rm ani}(R_{\rm CME}, t) \approx 30\left[1 + (f-1)\,e^{-\frac{1}{108}\left(\frac{R_{\rm CME}}{R_\odot}-1\right)}\right] \times \left(\frac{R_{\rm CME}}{R_\odot}\right)^{-0.4} \cos(\theta_{\rm CME})\,\mathcal{O}(t). \quad (17)$$

Here, $f = V^0_{\perp,\,\rm CME}/V_{\rm iso}$ is the CME-to-wind base speed ratio, and $\mathcal{O}(t)$ is the window function describing the CME's temporal intersection with the line of sight. Figure 4 shows (for a representative fast CME with $f = 3$, intersecting the line of sight at $R_{\rm CME} = 10\,R_\odot$) that the anisotropy factor reaches $\mathcal{B}_{\rm ani} \approx 34$, indicating a substantial enhancement in spectral broadening relative to ambient solar conditions.

4. Empirical Measurements of $\Delta\nu_{\rm sb}$

Over the years, numerous spacecraft have traversed superior conjunction—when the spacecraft passes behind the Sun relative to Earth—providing valuable opportunities to study the spectral broadening of narrowband carrier waves, which are part of the communication links, as they propagate through the solar corona and the IPM. These occultation events have enabled a wealth of empirical measurements that probe the electron-density fluctuations and associated scattering phenomena near the Sun. Thus, in this section, we examine perhaps the largest sample of important and significant observational measurements of spectral broadening. Our objectives are (a) to verify the radial dependence of $\Delta\nu_{\rm sb}$ given in Equation (11) using a larger sample of empirical spectral broadening measurements, and (b) to constrain the typical range of proportionality constants. We further show that the assumption of latitude independence in $\Delta\nu_{\rm sb}$ is consistent with these empirical observations.

Early radio occultation experiments with *Mariner IV* and *Pioneer 6* revealed that spacecraft signals at the *S* band (∼2.3 GHz) experienced noticeable spectral broadening—up to 9 $R_\odot$ from the Sun—with *Pioneer 6* data (R. M. Goldstein 1969) showing enhanced broadening during solar events. Later, the *Helios 1* and *2* missions extended these measurements down to 1.7 $R_\odot$ during solar minimum, confirming the trend of increasing broadening closer to the Sun (R. Woo & J. W. Armstrong 1979). The *Viking* mission further refined these observations by using dual-frequency (S- and X-band) measurements, reaching as close as 1.8 $R_\odot$ and 1.4 $R_\odot$, respectively, and enabling inferences on the power spectrum of electron-density fluctuations over a broad heliocentric range (R. Woo et al. 1976; R. Woo & J. W. Armstrong 1979). More recently, F. Azzollini et al. (2024) analyzed a large broadening dataset and described the radial dependence as a broken power law, with a steeper decline ($\sim r^{-2}$) below ∼3 $R_\odot$ and a flatter rate ($\sim r^{-1.7}$) beyond ∼10 $R_\odot$.

Figure 5 is perhaps the largest compilation of spectral broadening measurements from multiple sources, scaled to 1 GHz using the frequency scaling relation ($\nu^{-6/5}$). The data from R. M. Goldstein et al. (1967) correspond to *S*-band measurements taken during the superior conjunction of *Mariner IV*, which passed behind and slightly above the Sun, reaching within just a few solar radii. R. Woo et al. (1976) provided *S*-band measurements of spectral broadening from *Pioneer 6* over the range of ∼3–15 $R_\odot$, excluding transient solar events (R. M. Goldstein 1969). R. Woo (1978) reported *S*-band measurements from *Helios 1* and *Helios 2*, and additional Doppler scintillation measurements (which are proportional to spectral broadening) were made using *Helios 1*, *Pioneer 10*, and *Pioneer 11*, covering ∼2–200 $R_\odot$.

R. Woo & J. W. Armstrong (1979) contributed *S*- and *X*-band spectral broadening measurements from *Viking*, excluding a transient *S*-band event. The *L*-band measurements from *Venera 10* were provided by O. I. Yakovlev et al. (1980), and H. M. Bradford & D. Routledge (1980) observed spectral broadening from *Voyager 2* at the *S* band. A. I. Efimov et al. (2002) included *S*-band *Pioneer 10* and *L*-band *Venera 15/16* measurements. D. D. Morabito et al. (2003) detected broadening in signals from Cassini at both the *X* and *Ka* bands.

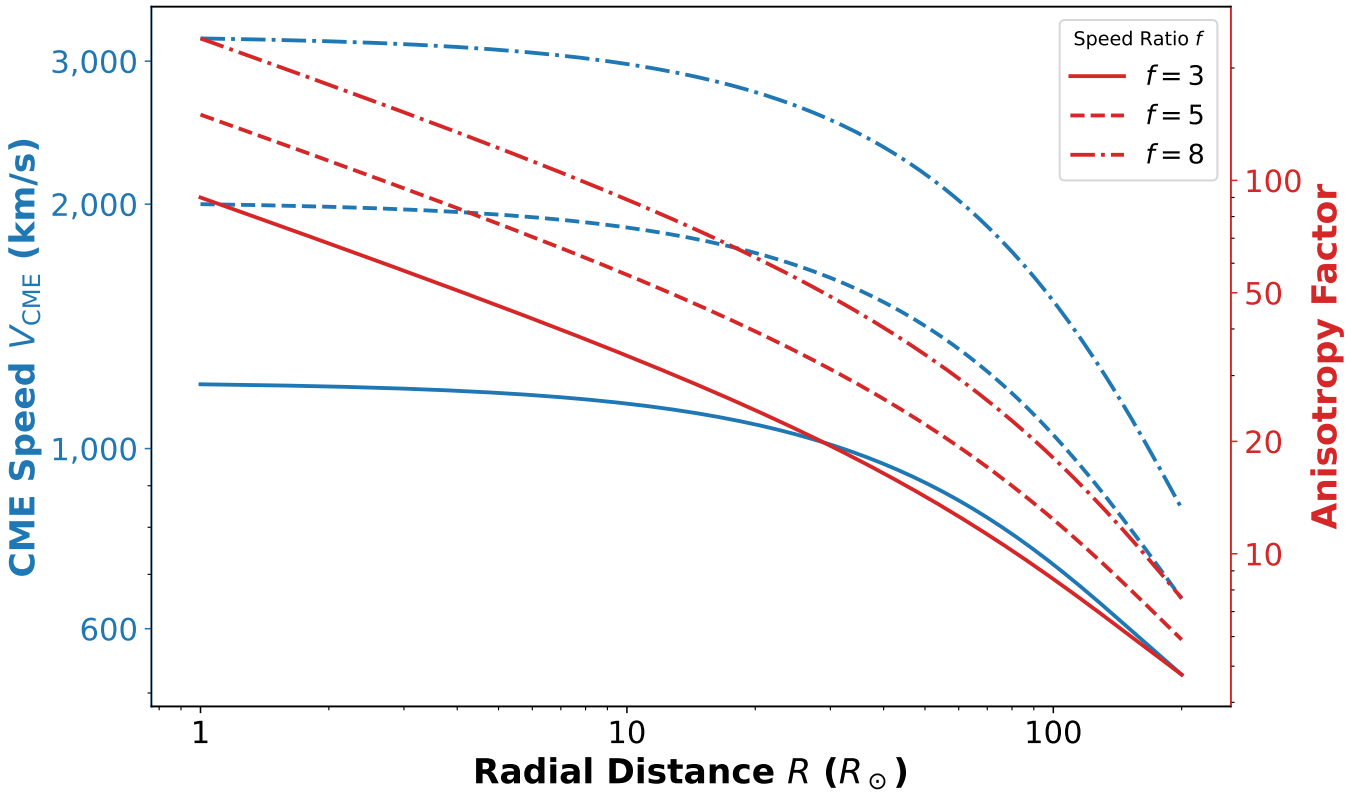

Figure 4. CME speed and anisotropy factor as a function of radial distance for three representative CME launch speed ratios: $f = V^0_{CME}/V_{iso} = 3$, 5, 8. The CME speed (blue curves, left y-axis) decreases with distance due to drag from the background wind, while the anisotropy factor $\mathcal{B}_{ani}$ (red curves, right y-axis) captures the transient enhancement in spectral broadening caused by CME-induced turbulence. The L_{drag} was assumed here as 0.5 au.

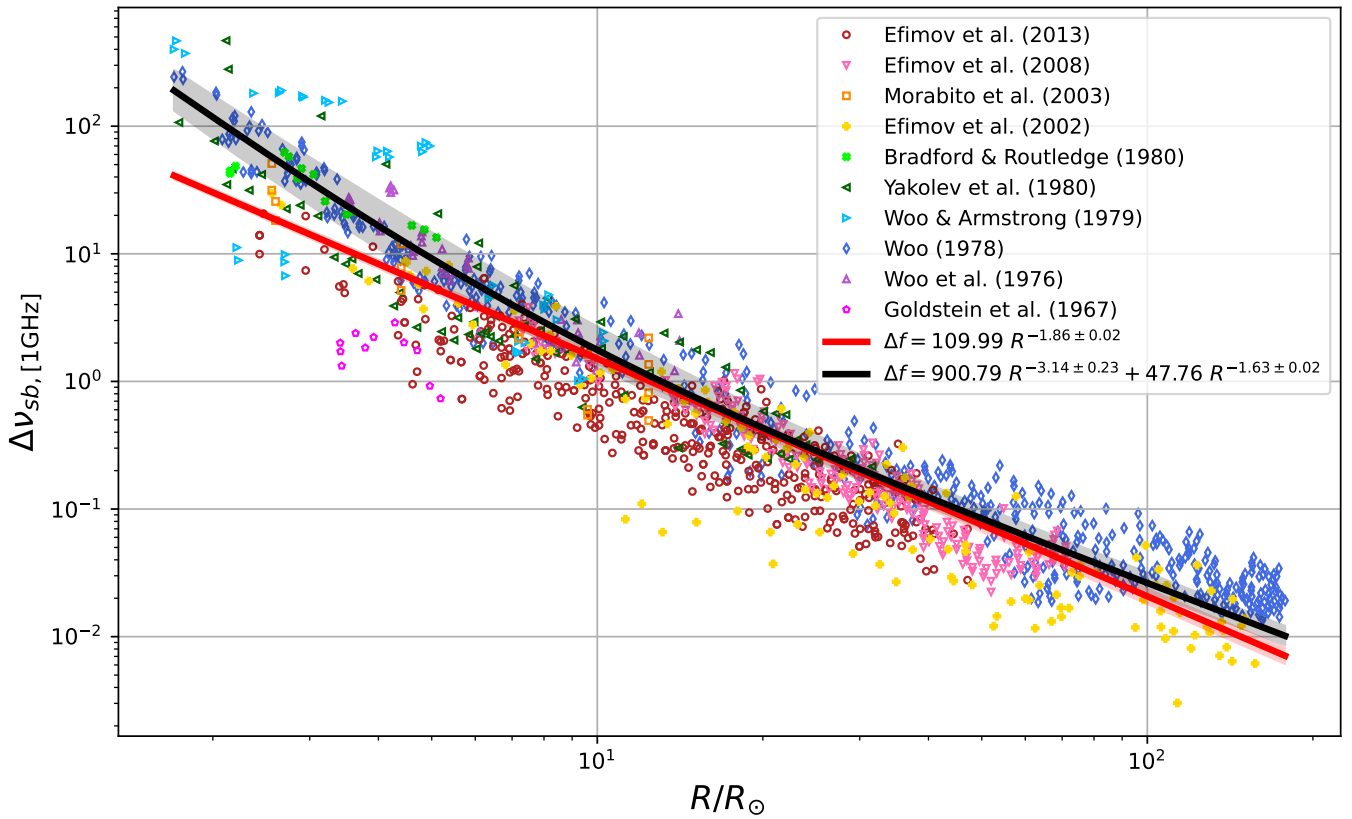

Figure 5. Recreation of Figure 2 from F. Azzollini et al. (2024). Spectral broadening measurements from several papers (R. M. Goldstein et al. 1967; R. Woo et al. 1976; R. Woo 1978; R. Woo & J. W. Armstrong 1979; H. M. Bradford & D. Routledge 1980; O. I. Yakovlev et al. 1980; A. I. Efimov et al. 2002, 2008, 2013; D. D. Morabito et al. 2003) scaled to 1 GHz by $\Delta\nu_{sb}/\nu \propto 1/\nu^{6/5}$ (instead of Azzollini's $\propto 1/\nu^2$). The break in the broken power law is set to 5 $R_\odot$.

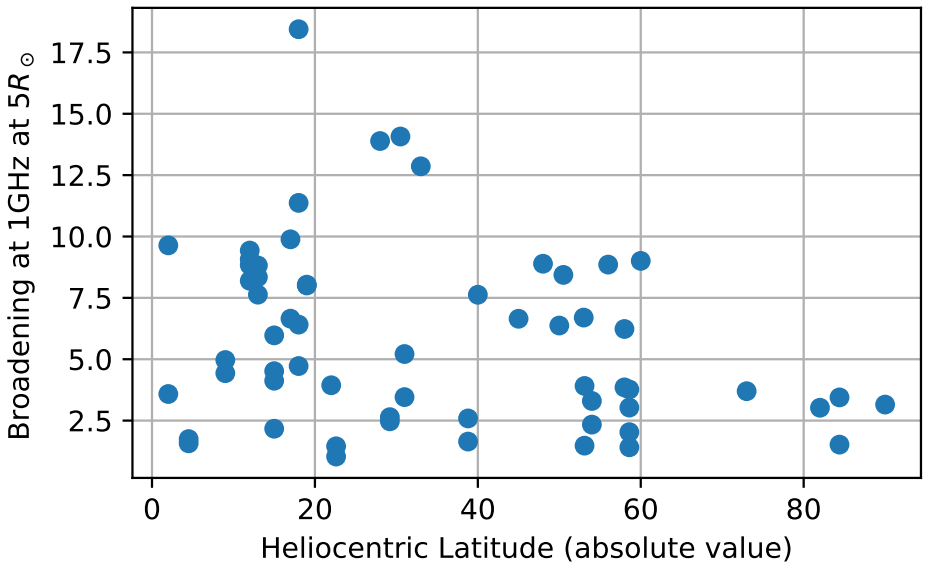

Figure 6. Latitude dependence of spectral broadening using measurements inferred from R. Woo et al. (1976), H. M. Bradford & D. Routledge (1980), D. D. Morabito et al. (2003), and A. I. Efimov et al. (2013). For all sources except A. I. Efimov et al. (2013), latitudes were inferred from the angle between the spacecraft's path and the Sun, as shown in figures in each paper. A. I. Efimov et al. (2013) included the maximum latitude for each conjunction in a table. Spectral broadening measurements were scaled to 1 GHz by $\Delta\nu_{\rm sb}/\nu \propto 1/\nu^{6/5}$ and then scaled to 5 $R_\odot$ by the broken power law in Figure 5.

A. I. Efimov et al. (2008) analyzed spectral broadening from *Galileo* at the *S* band, while A. I. Efimov et al. (2013) compiled data from *Mars Express*, *Venus Express*, and Rosetta missions with measurements in both the *S* and *X* bands.

Fitting a power law to the compiled data yields a relationship $\Delta\nu_{sb} \propto r^{-1.8}$, which remarkably matches our derived relation in Equation (11). When fitting a broken power law, we observe a steeper slope of $r^{-3.1}$ within $\sim$5 $R_\odot$, and a shallower slope of $r^{-1.6}$ beyond this distance. The break point at 5 $R_\odot$ was determined visually.

Most empirical evidence of spectral broadening in the solar system was taken during solar minimum, with only 15% of spectral broadening measurements being taken during the solar maximum. Fitting the two groups of measurements separately and fixing the slopes at -1.86, we find that solar maximum causes the coefficient to increase by $\sim$20 from solar minimum. The fit in Figure 5 lies right in the middle of the maximum and minimum fits.

Empirical evidence for the latitude dependence of spectral broadening remains limited, as relatively few studies explicitly report the heliographic latitude of their measurements. Figure 6 shows the inferred latitudes of spectral broadening observations from a subset of studies included in Figure 5, including R. Woo et al. (1976), H. M. Bradford & D. Routledge (1980), D. D. Morabito et al. (2003), and A. I. Efimov et al. (2013). These spectral broadening values were first normalized to 1 GHz using the frequency scaling relation (i.e., $\nu^{-6/5}$), and subsequently scaled to a common heliocentric distance of 5 $R_\odot$ using the broken power-law fit from Figure 5.

The most notable pattern in Figure 6 is the increased variance in spectral broadening at lower heliographic latitudes, compared to the relatively consistent values observed at higher latitudes. However, no clear or systematic trend in broadening as a function of latitude is evident from the data. This supports our earlier assumption that spectral broadening does not strongly depend on latitude, and justifies the use of a latitude-independent model for $\Delta\nu_{\rm sb}$ in our analysis (for Sun-like stars). Thus, utilizing these empirical measurements with the earlier derived relationship, the spectral broadening can be written for any Sun-like star as:

$$\Delta\nu_{\rm sb;\,\odot}(R,\,t) = \mathcal{B}_{\rm ani}(R,\,t)\;\nu_{\rm GHz}^{-6/5}\left(\frac{V_{\perp;\,\star}}{V_{\perp;\,\odot}}\right)\left(\frac{C^2_{n_e;\,\star}}{C^2_{n_e;\,\odot}}\right)^{3/5} \times\left[900.79\left(\frac{R}{R_\star}\right)^{-3.14} + 47.76\left(\frac{R}{R_\star}\right)^{-1.63}\right]\text{Hz} \tag{18}$$

where R is the impact distance of the line of sight from the star, $R_\star$ is the stellar radius, $\nu_{\rm GHz}$ is the observing frequency in GHz, and $V_\perp$ is the effective transverse speed, assumed constant for simplicity. A. P. V. Siemion et al. (2013) also reported similar frequency and radial dependence of spectral broadening. In summary, spectral broadening scales with electron-density fluctuations, stellar wind speed, and the turbulence scale, with faster winds and smaller-scale irregularities producing stronger effects. These dependencies, coupled with the empirical measurements, form the basis for modeling how the Exo-IPM may impact narrowband ETI signals we attempt to derive for M dwarf stars (largest concentration of stellar populations) in the next section.

5. M Dwarf Stars

M dwarf stars (dM) are the most ubiquitous in the Milky Way, with around three in four stars belonging to this class, some of them having been around since the early Universe (T. J. Henry & W.-C. Jao 2024). These long lifetimes suggest that such stars have had sufficient time to develop technologically advanced life (J. Tarter 2001; J. C. Tarter et al. 2007). Habitability around dM stars has been debated extensively due to tidal locking, high levels of X-ray/UV flux, and the potential for atmospheric stripping driven by frequent stellar flaring and CMEs (M. J. Heath et al. 1999; M. Lingam & A. Loeb 2017). However, J. C. Tarter et al. (2007) argued that tidal locking does not necessarily preclude habitability, as atmospheric and oceanic heat redistribution could mitigate

temperature extremes. A recent large study on dM stellar wind by B. E. Wood et al. (2021) suggested that previous assumptions on the high winds and CMEs damaging exoplanets around dMs might be overstated. Moreover, the sheer abundance and longevity of M dwarfs make them compelling candidates in the search for life-bearing worlds and, thus, the most important targets for the considerations of our work. In the following sections, we attempt to model ambient/isotropic stellar winds and turbulence environments in the Exo-IPM and compare them to empirical measurements from Sun-like stars as discussed in Section 4.

5.1. Steady M Dwarf Winds: $V_{\perp;\,dM}$

For all dM subtypes, magnetic fields play a crucial role in determining $V_{\perp;\,\mathrm{dM}}$ and $C^2_{\mathrm{n_e};\,\mathrm{dM}}$ in Equation (6) by transporting charged particles into the dM's Exo-IPM environment via Alfvén-wave-driven winds. A. L. Mesquita & A. A. Vidotto (2020) treated Alfvén waves as the sole driving mechanism in their dM wind simulations. Empirically, stellar winds in dM stars are constrained both through astrospheric Lyα absorption in the ISM (B. E. Wood et al. 2001) and via free–free emission from fully ionized outflows (M. Güdel 2002). A. A. Vidotto et al. (2011) modeled wind speeds up to 2300 km s^{-1} for the M4 dwarf V374Peg, while A. L. Mesquita & A. A. Vidotto (2020) predicted terminal speeds of 3100–3200 km s^{-1} for an M2 dwarf—approximately 8 times the solar value. T. Sakaue & K. Shibata (2021a) similarly found dM winds faster than the solar wind. T. Sakaue & K. Shibata (2021b) measured stellar wind as function of T_{eff}, which shows a trend of higher speed with lower temperatures of dMs (see Figure 5 in T. Sakaue & K. Shibata 2021b). In contrast, B. E. Wood et al. (2021), using high-resolution Hubble Space Telescope Lyα astrospheric observations, concluded that most dM stellar winds are weaker than or comparable to the solar wind. However, these constraints are derived at the astrospheric boundary under the assumption of steady-state winds and may not accurately reflect the dynamic conditions within the Exo-IPM—conditions most relevant to our spectral broadening analysis. Given these uncertainties, we adopt the following approximation in Equation (18), which spans the expected range from nonactive to highly active dMs:

$$V_{\perp;\mathrm{dM}} \approx (1 - 8)\, V^{\odot}_{\perp}\,. \tag{19}$$

Solar winds accelerate and then reach a terminal speed, which they maintain until entering the astrosphere. Alfvén-wave-driven models of dM winds exhibit a similar radial profile. V. Réville et al. (2024) showed that each simulation yields a wind speed profile reminiscent of solar-wind solutions. Hence, for our calculations, we assume a constant radial speed for the steady dM wind.

5.2. Strength of Turbulence in M Dwarfs: $C^2_{n_e;\,\mathrm{dM}}$

As outlined in Equations (4) and (6), the magnitude of spectral broadening also depends on $C^2_{n_e}$. To the best of our knowledge, there are no direct measurements or modeling of the level of turbulence in the dM's Exo-IPM environment. Hence, we must rely on other proxies that can inform us about possible levels of turbulence. As mentioned in Equation (8), $C^2_{n_e}$ can be approximated based on its relation to electron-density fluctuations (δn_e) and the turbulence outer scale (L_0).

For the solar wind, R. Woo (2007) and R. Woo & J. W. Armstrong (1979) have estimated $C^2_{n_e;\,\odot} \sim 10^{-4}$ m$^{-20/3}$ near 10 $R_{\odot}$, corresponding to fluctuation amplitudes $\delta n_{e;\,\odot}/n_{e;\,\odot} \sim 0.2$–$0.4$. In M dwarfs, especially active mid-to-late types, the situation is expected to be even more extreme: their enhanced coronal activity (N. Pizzolato et al. 2003), higher flare rates (J. Crowley et al. 2024), strong large-scale magnetic fields (J. Morin et al. 2010), and excess ionizing UV/X-ray photons (B. Stelzer et al. 2013; S. G. Engle 2024) all support elevated density fluctuations.

Direct measurements of δn_e around dMs do not yet exist, but Alfvén-wave-driven simulations by T. Sakaue & K. Shibata (2021b) provide useful guidance. Their 1D magnetohydrodynamics (MHD) model yields rms transverse speeds $v_{\phi} \simeq 100$–150 km s^{-1} at a sound speed $c_s \simeq 120$ km s^{-1}, i.e., a turbulent Mach number $M_t = v_{\phi}/c_s \simeq 0.8$–$1.2$. Recent high-resolution observations from NASA's Magnetospheric Multiscale Mission and compressible-MHD simulations demonstrate that the fractional density fluctuation scales linearly with the turbulent Mach number $\delta n_e/n_e = b\,M_t$, with $b \approx 0.3$–1 depending on the relative compressive/solenoidal driving (R. Bandyopadhyay et al. 2025). Applying this empirical relation to the T. Sakaue & K. Shibata (2021b) speeds gives $\delta n_e/n_e \simeq 0.3$–$1.2$, a factor of $\sim$2–4 above the near-Sun solar-wind value. B. E. Wood et al. (2021) reported $\dot{M}_{\mathrm{dM}} \sim 0.1 - 30\,\dot{M}_{\odot}$ (median $\simeq 0.5\,\dot{M}_{\odot}$), implying $n_{e;\,\mathrm{dM}} \approx 0.5\,n_{e;\odot}$ at equal radii. Adopting the empirical scaling $\delta n_e/n_e = bM_t$ (R. Bandyopadhyay et al. 2025) with $b \in [0.3, 1]$, $M_t^{\mathrm{dM}} \sim 0.8 - 1.2$, and $M_t^{\odot} \sim 0.3$ yields $\delta n_{e;\mathrm{dM}} \approx 0.4 - 7\,\delta n_{e;\odot}$, from slightly below to an order of magnitude above near-Sun perturbations, with the mid-range ($\sim$1×–3×) most likely if both winds are driven by mixed Alfvénic and compressive turbulence.

For dMs, outer turbulence scales are expected to be smaller than in the solar corona because their magnetically confined coronae are more compact and energetic (A. Reiners et al. 2009; J. Morin et al. 2010). Wind models reinforce this: A. L. Mesquita & A. A. Vidotto (2020) adopted dissipation lengths of $\sim 0.1\,R_{\star}$, while the 3D MHD simulations of A. A. Vidotto et al. (2013) place the Alfvén surface at only 2–3 $R_{\star}$, implying injection scales $\lesssim 0.2\,R_{\star}$. Enhanced non-thermal UV/X-ray variability in dMs (B. Stelzer et al. 2013; S. G. Engle 2024) further signals vigorous small-scale magnetic activity and, by extension, stronger turbulence. Adopting fractional density fluctuations $\delta n_{e;\mathrm{dM}}/\delta n_{e;\odot} \simeq 0.4$–$7$ and outer-scale ratios $L_{0,\mathrm{dM}}/L_{0,\odot} \simeq 0.2$–$0.5$, the scaling $C^2_{n_e}$ from Equation (8) implies an enhancement ranging from ~ 0.3 to $\sim 1.5 \times 10^2$ times the solar value, with the most probable regime ($\delta n_{e;\mathrm{dM}}/\delta n_{e;\odot} \sim 2$–$4$ and $L_{0,\mathrm{dM}}/L_{0,\odot} \sim 0.3$) yielding a factor of $\sim$5–30. We therefore write

$$C^2_{n_e;\mathrm{dM}} \;\approx\; (0.3 - 150)\, C^2_{n_e;\odot}, \tag{20}$$

which captures both typical and extreme expectations for scattering strength in dM Exo-IPM environments.

A. L. Mesquita & A. A. Vidotto (2020) assumed that the electron density around the dM has a similar profile to that observed in the solar wind: $\propto r^{\sim -2}$, consistent with the Parker wind theory (E. N. Parker 1958). Furthermore, in Alfvén-wave-driven winds, the nonlinear cascade is initiated near the Alfvén radius, introducing a break in the radial turbulence profile (also verified by previous empirical measurements outlined in Figure 5), which appears to be similar for the Sun

and dMs (A. L. Mesquita & A. A. Vidotto 2020). Hence, we can assume $C^2_{n_e;\mathrm{dM}}$ to have the same radial dependence as Equation (8).

5.3. Latitude Dependence of $V_{\perp;\,dM}$ and $C^2_{n_e;\,\mathrm{dM}}$

V. Réville et al. (2024) demonstrated from their Alfvén-wave-driven MHD simulations that M dwarf winds exhibit a latitude dependence similar to that of the Sun. Open-field polar regions launch a fast, low-density wind ($V^{\mathrm{pol}}_{\perp;\,\mathrm{dM}} \sim 2 - 3 \times 10^2$ km s^{-1}), whereas the closed-field equatorial streamer belt produces a slower, denser outflow ($V^{\mathrm{eq}}_{\perp;\,\mathrm{dM}} \sim 0.5 - 1 \times 10^2$ km s^{-1}). Hence, as noted in Section 2.3 and confirmed by empirical observations in Section 4, the opposing latitude dependences of $V_{\perp;\,\mathrm{dM}}$ and $C^2_{n;\,\mathrm{dM}}$ may largely cancel. For our order-of-magnitude estimates, we therefore neglect latitude dependence and treat spectral broadening as a function of radius only.

5.4. Anisotropy due to CMEs in dM

As discussed in Section 3, transient CMEs can enhance spectral broadening through their turbulent sheaths. Although one might expect an even stronger anisotropic contribution in active M dwarfs—given their high flare rates and strong magnetic fields—both theoretical work (J. D. Alvarado-Gómez et al. 2018) and observational evidence (K. Vida et al. 2019) suggest that CMEs on dM stars are not fundamentally more disruptive to wave propagation than solar CMEs, as discussed in detail in Section 3.

For dM stars, the scarcity of direct detections and the limited number of indirect signatures mean that we cannot provide a detailed quantitative estimate of the contributions from individual terms (i.e., $V^{\mathrm{dM}}_{\perp;\,\mathrm{CME}}$, $\delta n^{\mathrm{dM}}_{e;\,\mathrm{CME}}$, and $L^{\mathrm{dM}}_{0;\,\mathrm{CME}}$) like we did for the solar CMEs. Strong large-scale magnetic fields in dM stars can confine plasma and suppress many eruptions before they escape, leading to a lower effective CME rate than one would predict from flare occurrence alone (P. Odert et al. 2017; J. D. Alvarado-Gómez et al. 2018). The CMEs that do escape do not appear systematically faster than solar CMEs: speeds inferred from Balmer-line asymmetries are typically a few hundred to a thousand kilometers per second, comparable to solar values ($V^{\mathrm{dM}}_{\perp,\mathrm{CME}} \approx V^{\odot}_{\perp,\mathrm{CME}}$; K. Vida et al. 2019; M. Leitzinger et al. 2024). The lack of confirmed stellar Type II radio bursts is consistent with most events being sub-Alfvénic and unable to drive strong shocks (M. K. Crosley & R. A. Osten 2018). Indirect evidence of mass ejection is provided by transient Balmer-line asymmetries (K. Vida et al. 2019; J. Wang et al. 2021) and by coronal dimmings in X-ray and extreme-UV bands (A. M. Veronig et al. 2021). A few individual events have implied masses up to 10^{17}–10^{18} g (C. Argiroffi et al. 2019; J. Wang et al. 2021), which lie at the high end of the solar CME distribution but are not clearly distinct in their impact on propagation. Moreover, dM wind mass-loss constraints from astrospheric Lyα absorption and, more recently, from LOFAR free–free absorption limits (S. Bloot et al. 2025) argue against an unchecked population of massive CMEs, as solar flare–CME scaling would otherwise overpredict $\dot{M}$ by orders of magnitude (P. Odert et al. 2017; S. Bloot et al. 2025). This in turn suggests that the turbulence environment of dM CMEs is broadly similar (on the order-of-magnitude scale) to the solar case (i.e., $C^{2,\,\mathrm{dM}}_{n_e,\mathrm{CME}} \approx C^{2,\,\odot}_{n_e,\mathrm{CME}}$). Taken together, these arguments indicate that while CMEs do occur on M dwarfs, their occurrence rate is moderated by magnetic suppression, and their per-event properties are not systematically more extreme than solar. We therefore adopt the same anisotropy factor derived for solar CMEs (see Section 3), $\mathcal{B}^{\mathrm{dM}}_{\mathrm{ani}} \approx \mathcal{B}^{\odot}_{\mathrm{ani}}$, without introducing any additional enhancement for dM stars.

5.5. Spectral Broadening: $\Delta\nu_{sb;\,dM}$

We now attempt to combine the assumptions derived in Equations (19) and (20) for the expected spectral broadening from the Exo-IPM around dM stars, and rewrite Equation (18). Of course, there are no empirical measurements of spectral broadening from the Exo-IPM of dM stars. However, given that we have normalized the contributing quantities with the similar radial relationship, we can, for brevity, adopt the same form of the equation with normalization factors applied as:

$$\Delta\nu_{\mathrm{sb;\,dM}}(R,\,t) = \mathcal{B}^{\mathrm{dM}}_{\mathrm{ani}}(R,\,t)\;\nu^{-6/5}_{\mathrm{GHz}}\left(\frac{V_{\perp;\,\mathrm{dM}}}{V_{\perp;\,\odot}}\right)\left(\frac{C^2_{n_e;\,\mathrm{dM}}}{C^2_{n_e;\,\odot}}\right)^{3/5} \times\left[900.79\left(\frac{R}{R_\star}\right)^{-3.14} + 47.76\left(\frac{R}{R_\star}\right)^{-1.63}\right]\mathrm{Hz} \tag{21}$$

Figure 7 shows a comparison between the solar system IPM and the Exo-IPM around a typical dM star under steady-state conditions, using Equations (18) and (21). As is clearly evident from these equations, the expected spectral broadening of a passing narrowband signal is a strong function of both radial distance and observing frequency. Sub-GHz frequencies are particularly impacted, especially when the line of sight passes within a few tens of stellar radii. This is a significant finding that, to the best of our knowledge, has not been previously discussed in the literature. It has the potential to substantially affect detection capabilities at GHz and sub-GHz frequencies for a large number of potential sources.

It should be noted that Figure 7 represents only the ambient steady wind conditions. If we consider a scenario in which an ejected CME event passes directly transverse to the line of sight, as described in Equation (17), the expected spectral broadening from dM stars could be up to 10^3 times greater than the already elevated ambient levels shown in Figure 7. In the following section, we explore these probabilistic scenarios further, along with the effects of different orbital configurations.

6. Simulated Technosignature Survey of Nearby Million Stars

6.1. Orbital Parameters

As outlined in Sections 4 and 5.5, spectral broadening varies as a function of the impact distance between the line of sight and the host star. In our simplified modeling shown in Figures 1 and 3, and discussed in Section 5.5, we assumed a transmitter orbiting a typical M dwarf in a perfectly circular orbit observed in an edge-on configuration. However, the actual orbits of potential transmitters located on the surface of exoplanets are likely to span a broad range of orbital parameters, including eccentricity, inclination, semimajor axis, argument of periastron, and true anomaly. Figure 8 outlines some of the example projected orbits for different configurations of orbital parameters. For any given planetary system, the impact distance R_{imp}, which is the closest distance from the

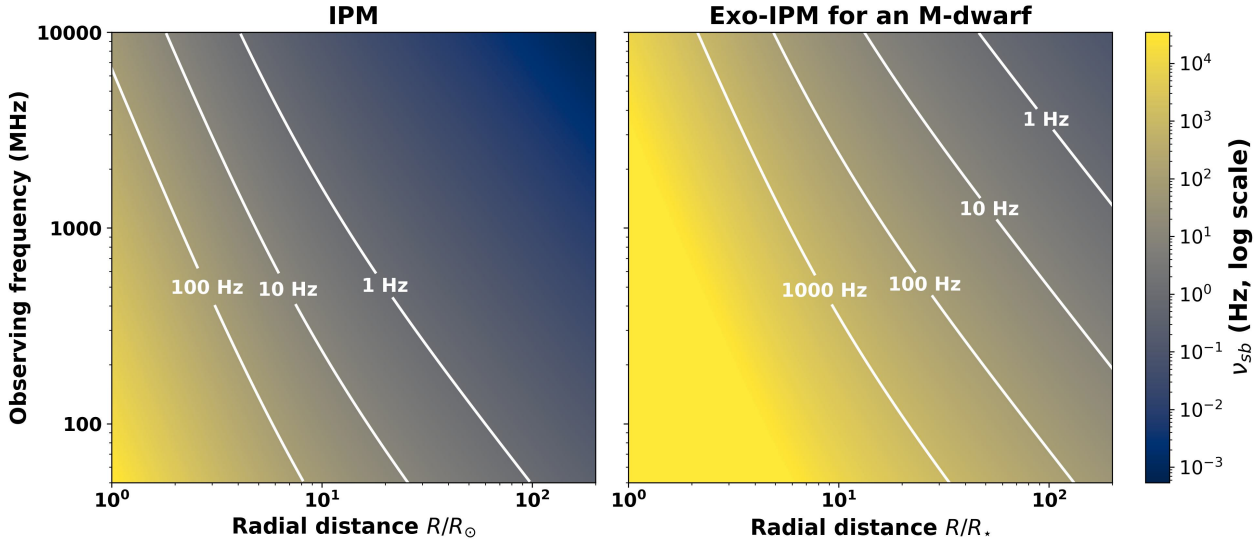

Figure 7. Spectral broadening $\Delta\nu_{\rm sb}$ as a function of radial distance and observing frequency for (a) the solar IPM and (b) a typical dM Exo-IPM, assuming no anisotropy but adopting the higher end of the normalization parameters ($V_\perp/V_{\perp,\odot}$ and $C^2_{n_e}/C^2_{n_e,\odot}$) from Equations (19) and (20). Both panels share the same log-scaled color bar (normalized to the solar case), with overlaid white contours marking constant $\Delta\nu_{\rm sb}$ levels. For the dM Exo-IPM, it is evident that a planet as far as 200 stellar radii can experience several hertz of spectral broadening at GHz frequencies, increasing to hundreds of hertz as the planet moves into superior conjunction.

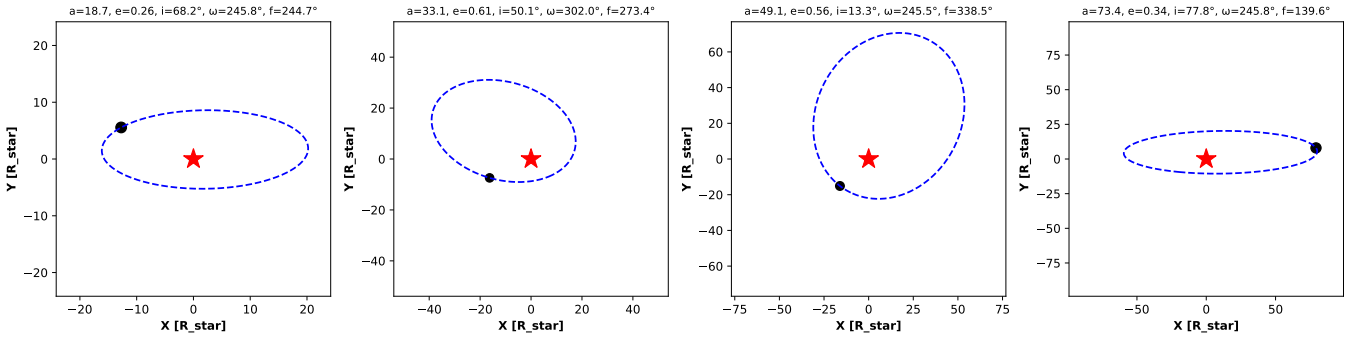

Figure 8. Examples of projected orbital configurations of exoplanets around an M dwarf star, sampled from a Monte Carlo simulation spanning a range of orbital parameters. Each panel shows the orbit (blue dashed line), the host star at the origin (red star), and the instantaneous location of the planet (black circle) at a randomly selected true anomaly. Orbital elements such as semimajor axis (a), eccentricity (e), inclination (i), argument of periastron (ω), and true anomaly (f) are indicated in each title. These variations illustrate the diversity of possible impact distances mentioned in Equations (18) and (21).

line of sight to the star, can be calculated as

$$R_{\rm imp}\,(f) = \frac{a(1-e^2)}{1+e\cos f}\,\sqrt{1-\sin^2 i\,\sin^2(\omega+f)}\,. \qquad (22)$$

Here, a is the semimajor axis, e is the eccentricity, i is the inclination, ω is the argument of periastron, and f is the true anomaly. We have only considered the impact distance for the cases when the planet is behind the star. As shown in Equation (18) and Figure 7, even modest changes in impact distance can result in significant differences in spectral broadening due to its steep radial dependence near the host star.

We modeled a wide range of orbital parameters to sample a variety of different projected orbital configurations. These variations introduce important diversity in the expected $\Delta\nu_{\rm sb}$ and must be accounted for in realistic technosignature searches. Figure 9 shows spectral broadening as a function of orbital phase (i.e., fraction of the orbit) for a range of orbital configurations. It shows how spectral broadening increases sharply near superior conjunction as the planet approaches the star, particularly for smaller orbital distances. Figure 9 also demonstrates the influence of increasing orbital eccentricity, inclination effects, and the impact of rotating the orbit within the plane. For example, as is evident in the top-right plot of Figure 9, in a highly elliptical orbit—where the planet moves fastest at periastron—an inclination of 90° can yield very different fractions of the orbit experiencing strong spectral broadening, depending on the argument of periastron (e.g., 0° versus 90°).

6.2. Encounters with CMEs

As indicated in Equation (17) and Section 5.4, a CME crossing the line of sight can enhance spectral broadening by a factor of 10–100 (see Figure 3) in Sun-like and dM stars. Such strong scattering can broaden a passing technosignature beyond detectability. It is therefore essential to quantify both the CME occurrence rate and the probability of geometric interception. The encounter probability depends on (a) the median CME rate $\lambda_{\rm CME}$ (events day^{-1}), (b) the CME opening angle $\Omega_{\rm CME}$, (c) the observation duration $T_{\rm obs}$, and (d) the CME active duration $\tau_{\rm CME}$. If $\tau_{\rm CME} \gg T_{\rm obs}$ (typical length of

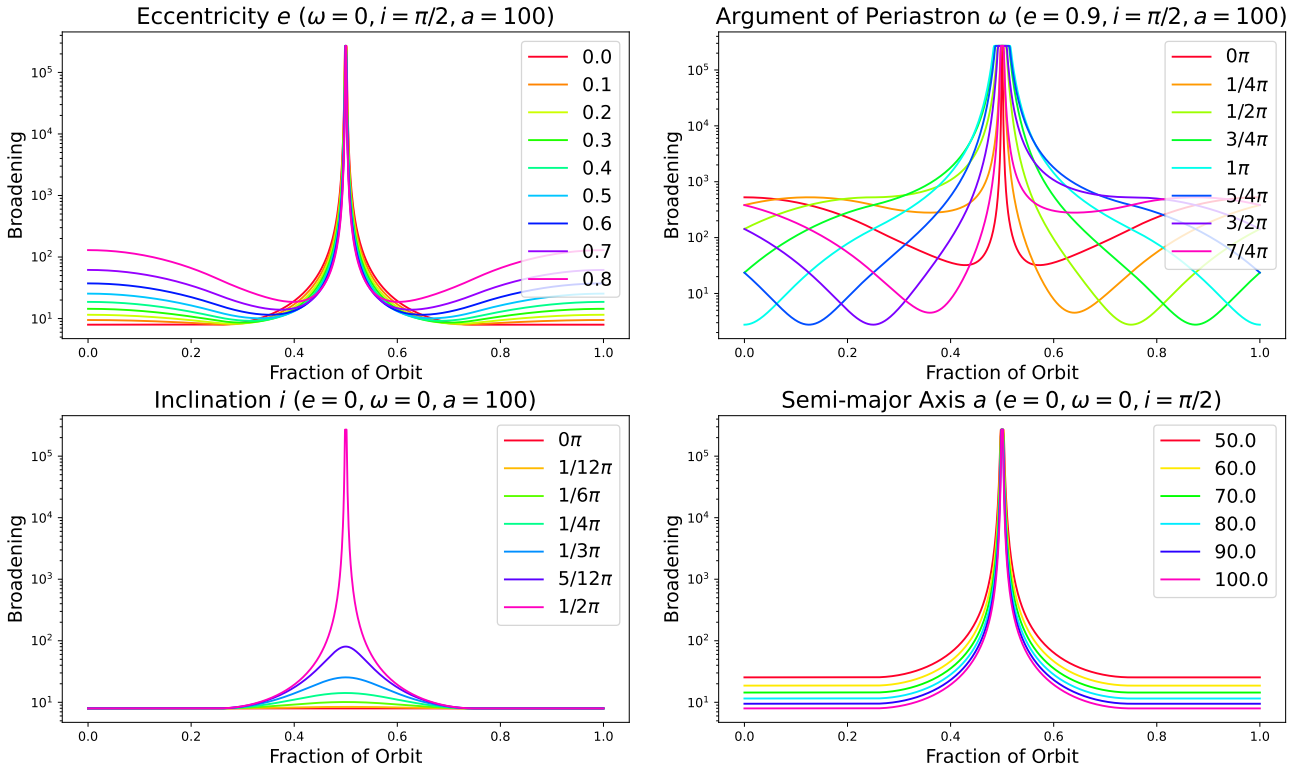

Figure 9. Spectral broadening of a narrowband transmitter at 1 GHz as function of orbital phase for a sample of different orbital configurations. Each panel isolates the effect of varying one orbital element—eccentricity e, argument of periastron ω (in radians), inclination i (in radians), or semimajor axis a (in $R_\star$)—while keeping the others fixed. For each configuration, the Doppler-induced spectral broadening is computed at 1000 points evenly spaced across a full orbit using the formalism developed in Section 5.5.

observations), the explicit dependence on $T_{\rm obs}$ can be neglected. M. S. Wheatland (2003) analyzed LASCO statistics and showed that CME wait times are consistent with a time-dependent (solar-cycle-modulated) Poisson process; over short intervals treated as stationary, the inter-arrival distribution is $P(\Delta t|\lambda) = \lambda e^{-\lambda \Delta t}$ with $\lambda(t)$ varying across the cycle. S. Yashiro et al. (2004) reported typical active durations $\tau_{\rm CME} \sim 8$–10 hr. No direct correlation between $\lambda_{\rm CME}$ and $\tau_{\rm CME}$ was identified, so we treated CME occurrences as independent, memoryless events.

For the CME encounter statistics used in this work, we performed an end-to-end Monte Carlo over the relevant parameter space. For each simulated system and epoch, we drew a CME start time uniformly within a padded window $[-2T_{\rm obs}, 2T_{\rm obs}]$, and assigned a duration $\tau_{\rm CME}$ from an empirical Gamma distribution (2–48 hr, mean $\sim$8 hr; S. Yashiro et al. 2004). The opening angle $\Omega_{\rm CME}$ was sampled from a log-normal distribution spanning 10°–180°, and the CME speed $V_{\rm CME}$ from a Weibull distribution covering 80–2300 km s^{-1} (both from S. Yashiro et al. 2004). Given the transmitter's instantaneous orbital state, an encounter was recorded only when (i) the CME was temporally active during the observation and (ii) its cone intercepted the transmitter–observer line of sight (Figure 3). The resulting encounter fraction was then used to weight the $\mathcal{B}_{\rm ani}$ enhancement in Equation (17).

6.3. Monte Carlo Simulations across Stellar Types

To evaluate the probabilistic impact of stellar environments on technosignature detectability, we performed a Monte Carlo simulation of a hypothetical technosignature search toward 10^6 exoplanetary systems consisting of 25% Sun-like stars and 75% dMs. Each system was assigned a random set of orbital parameters—including semimajor axis, eccentricity, inclination, argument of periastron, and true anomaly. Table 1 lists all of the prior distributions and their corresponding ranges considered in this simulation. For Sun-like stars, we simulated transmitter orbits with semimajor axes ranging from 10 stellar radii to 1 au. In contrast, for M dwarfs—where planets are typically found much closer to their host stars—we restricted the semimajor axis range to 10–100 stellar radii, corresponding to the outer edge of the habitable zone around a representative dM star.[5]

For each orbital realization, we computed the sky-projected impact distance between the transmitter and the host star using the formalism described in Figure 1. This distance was then mapped to an expected spectral broadening value using Equation (18) for Sun-like stars and Equation (21) for dMs. For dMs, we additionally drew random values for ambient stellar wind speeds (see Section 5.1) from the range outlined in Equation (19) and turbulence strengths (see Section 5.2) from Equation (20). For each case, we also simulated a range of CME parameters, including a uniform distribution of their longitude and latitude of origin, opening angles, speed (Section 3.1), turbulence strength (Section 3.2), active duration, and start time relative to the observations. Based on these selections, if the line of sight toward the random location of the transmitter in its orbit happened to pass through a CME cone, we multiplied the corresponding $\mathcal{B}_{\rm ani}$ factor with

[5] For example, all of the habitable planets around the Trappist-1 star are well within this range.

Table 1
Simulation Parameters and Priors Used in the Monte Carlo

Parameter	Range/Prior (Distribution)
Stellar population	
Sun-like : dM fraction	0.25 : 0.75 (categorical)
dM stellar and turbulence parameters	
Stellar radii $R_{\rm dM}$	$\mathcal{U}[0.08,\ 0.7]\ R_{\odot}$
Mass $M_{\rm dM}$	$\mathcal{U}[0.1,\ 0.6]\ M_{\odot}$
Isotropic Winds $V_{\perp}^{dM}$	$\mathcal{U}[1,\ 8]\ V_{\perp}^{\odot}$
Strength of turbulence $C^2_{n_e;dM}$	$\mathcal{U}[0.3,\ 150]\ C^2_{n;\odot}$
Orbital elements	
Semimajor axis a (Sun-like)	Log-uniform on $[10,\ 217]\ R_{\star}$
Semimajor axis a (dM)	Log-uniform on $[10,\ 100]\ R_{\star}$
Eccentricity e	$\mathcal{U}[0,\ 0.9]$
Inclination i	Isotropic: $\cos i \sim \mathcal{U}[0,\ 1]$, $i \in [0,\ \pi]$
Longitude of ascending node Ω	$\mathcal{U}[0,\ 2\pi)$
Argument of periastron ω	$\mathcal{U}[0,\ 2\pi)$
True anomaly f	$\mathcal{U}[0,\ 2\pi)$ (random location of transmitter in the orbit)
CME parameters	
Start time (relative to observation)	$\mathcal{U}[-2T_{\rm obs},\ 2T_{\rm obs}]$
Active duration $\tau_{\rm CME}$	Gamma($k = 4$, mean $\approx$ 8 hr), truncated to [2, 48] hr
Opening angle (apparent width)	Log-normal; 10°–180°
Speed $V_{\rm CME}$	Weibull; 80–2300 km s^{-1}
CME stellar longitude	$\mathcal{U}[0,\ 2\pi)$
CME stellar latitude	$\mathcal{U}[-\pi/2,\ +\pi/2]$

Note. Monte Carlo priors for stellar mix, orbital parameters, and CME events are adopted for the simulated technosignature survey of 1 million nearby stellar systems. The ranges of different parameters are shown together with their corresponding random distribution formats. In most cases, parameters are drawn from uniform distributions ($\mathcal{U}$), since their true underlying distributions remain largely unknown.

the spectral broadening already present due to the ambient medium.

The distribution of spectral broadening was examined for two observing frequencies: 1 GHz and 100 MHz. The survival functions (i.e., complementary cumulative distribution functions, CDFs) of the resulting spectral broadening values are shown in Figures 10 and 11. These curves describe the probability that a randomly selected system will exhibit spectral broadening greater than a given threshold $\Delta\nu_{\rm sb}$. The survival function is defined as

$$S(\Delta\nu_{\rm sb}) = \mathbb{P}(\text{Broadening} > \Delta\nu_{\rm sb}) = 1 - F(\Delta\nu_{\rm sb}), \quad (23)$$

where $F(\Delta\nu_{\rm sb})$ is the CDF of spectral broadening values. These functions are constructed from our Monte Carlo simulations by sorting the computed broadening values in descending order and assigning a survival probability proportional to the rank within the population. At 1 GHz, more than 70% of systems exhibit some degree of broadening, with over 30% showing $\Delta\nu_{\rm sb} \geqslant 10$ Hz—posing a significant challenge on their detectability by conventional narrowband search pipelines (J. E. Enriquez et al. 2017; J.-L. Margot et al. 2018) tuned to detect sub-Hz δ-like lines. At 100 MHz, the problem becomes even more severe: nearly 60% of systems show broadening of $\Delta\nu_{\rm sb} \geqslant 100$ Hz. From these simulations, we conclude that among 10^6 nearby stars, if even one hosts a transmitter, there is a >30% chance that its signal will be broadened by at least 10 Hz at 1 GHz, and a >60% chance of broadening beyond 100 Hz at 100 MHz. We further conclude that encounters with CMEs can increase the spectral broadening by an order of magnitude. However, due to geometric constraints, the probability of such encounters is relatively low ($\leqslant$3%).

7. Discussion

7.1. The "Great Silence"

Narrowband technosignature searches have been pursued for over six decades, historically concentrated near 1.4 GHz (G. Cocconi & P. Morrison 1959) and, more recently, extended to lower frequencies (e.g., LOFAR, MWA; S. J. Tingay et al. 2016; O. A. Johnson et al. 2023). These signals are expected to drift in frequency (exhibiting $\dot{\nu}$) due to relative Doppler motion between transmitter and receiver. Efficient Taylor-tree algorithms applied to the highest spectral resolution data products are typically used to search for these narrowband drifting signals (J. E. Enriquez et al. 2017; J.-L. Margot et al. 2018). Most analyses translate nondetections into limits on the effective isotropic radiated power (EIRP) under an implicit assumption of an intrinsically δ-function (or $\sim$1 Hz) linewidth (J. E. Enriquez et al. 2017; D. C. Price et al. 2020; V. Gajjar et al. 2021). Although SETI@HOME searched across different narrowband signals with widths ranging from 0.07–1221 Hz, this was only over just 2.5 MHz of the total bandwidth (E. J. Korpela et al. 2025). Our results challenge the premise of intrinsic δ-like signals, as turbulence in the Exo-IPM generically imposes Lorentzian-like spectral broadening that redistributes power from any putative intrinsic δ-shaped narrowband signal into extended wings. This suppresses the peak S/N that standard narrowband pipelines rely upon. For a $\mathcal{W}_0$ Hz intrinsic top-hat signal with amplitude $\mathcal{A}$, the peak-loss factor scales as $\mathcal{A} \times \frac{2}{\pi}\arctan(\mathcal{W}_0/\Delta\nu_{\rm sb})$ for a Lorentzian-broadened spectral line. For comparison, if we assume intrinsic width of the transmitted signal is 1 Hz, then the degradation in the peak flux density will be of the order of 94% as that signal gets spectrally broadened to 10 Hz (retaining only 6% of the original peak S/N). As reported in Section 6.3, at GHz frequencies, a substantial fraction (>30%) of systems in the solar neighborhood exhibit broadening >10 Hz, while at 100 MHz, broadening of the order of $\gtrsim$100 Hz is common (affecting close to 60% of systems). In such cases, peak-based detectors can simply miss broadened signals even when the integrated flux density remains detectable. Furthermore, as highlighted in Section 6.3, anisotropy imparted by coincident transient CMEs can completely wipe out passing narrowband signals in a small but significant fraction of systems. Hence, the so-called Great Silence (G. D. Brin 1983), when extended to the radio technosignature searches, is not solely evidence for the absence of transmitters, but also a reflection of our detection limitations arising from a *mismatch* between the assumed signal morphology and the broadened line shapes induced by the Exo-IPM. It is beyond the scope of this work to quantify the true impact of this broadening on existing

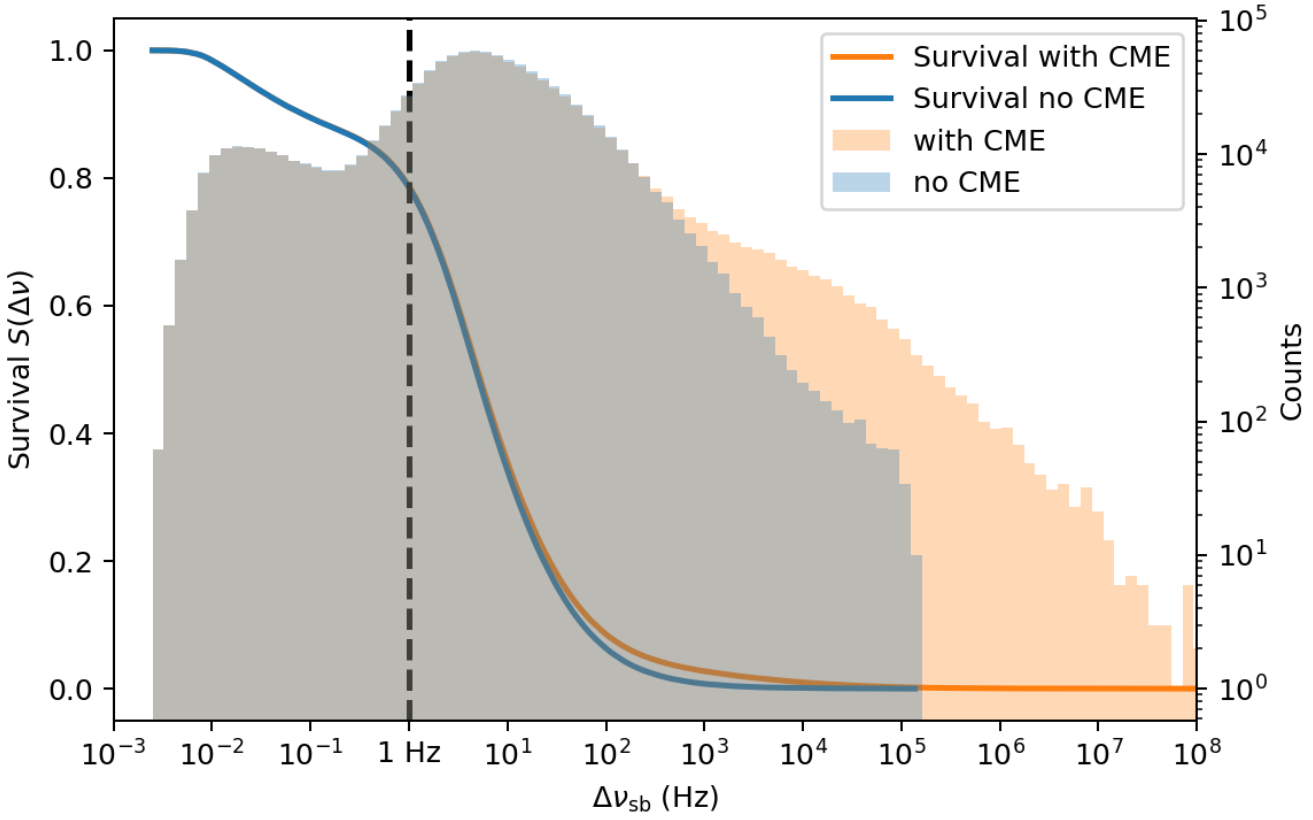

Figure 10. Distribution of expected spectral broadening of narrowband radio signals at 1 GHz computed from a Monte Carlo simulation of 10^6 planetary systems in a mixed stellar population comprising 25% Sun-like stars and 75% M dwarfs. The histograms show the distribution of spectral broadening across simulated Exo-IPM environments for a transmitter on orbits spanning a wide range of orbital properties and sky-projected orientations. The curve shows the survival function—with and without CMEs—giving the probability that a randomly selected system from the solar neighborhood will exhibit spectral broadening greater than a given threshold. Spectral broadening incurred during CME encounters is shown separately, which highlights that due to geometry, <3% of systems are impacted. Overall, >75% of systems experience some degree of spectral broadening, with ∼30% experiencing ⩾10 Hz, degrading the detected transmitted power by 94% (i.e., $\frac{2}{\pi}\arctan(0.1) \sim 6\%$).

narrowband search algorithms and reported constrain on the targeted stellar populations on all previous surveys; we aim to address this in subsequent studies (G. C. Brown & V. Gajjar 2026, in preparation).

7.2. Broadening Aware Technosignature Searches

B. Brzycki et al. (2023) and B. Brzycki et al. (2024) discussed using IPM scintillation to discriminate between RFI and narrowband technosignatures. Similarly, spectral line shape changes imparted by the Exo-IPM can be exploited to distinguish truly sky-originating signals from terrestrial interference. Spectral broadening and the associated diffractive scintillation on a timescale $t_{\rm diff} \sim (\pi\ \Delta\nu_{\rm sb})^{-1}$ are strong indicators that a signal is being produced by an exoplanet orbiting a representative stellar population. Moreover, the dependence of spectral broadening on orbital phase can serve as a powerful diagnostic for confirming whether a signal originates from a known exoplanet system in targeted observations. For example, recent observations with the Five-Hundred-Meter Aperture Spherical Telescope of the TRAPPIST-1 system (G.-Y. Song et al. 2025) could have been informed by orbital-phase predictions: TRAPPIST-1 is a very active star, and the close-in orbits of its planets suggest that any narrowband transmission would likely be broadened.

We therefore recommend that future surveys treat linewidth as a fundamental search parameter. Pipelines should deploy width-aware matched filters spanning both Doppler drift and spectral broadening ($\dot{\nu}$, $\Delta\nu_{\rm sb}$). We also recommend multi-resolution channelizations to maintain sensitivity across decades in $\Delta\nu_{\rm sb}$. For example, the SETI@HOME pipeline actually carried out searches across multiple spectral resolutions, ranging from 0.07–1221 Hz, which would be an ideal approach (E. J. Korpela et al. 2025). Rather than reporting EIRP sensitivities for δ-function narrowband signals, surveys should present sensitivity surfaces $S_{\rm min}(\dot{\nu}, \Delta\nu_{\rm sb})$, with EIRP limits marginalized over width priors informed by stellar type and orbital geometry for targeted searches. Observing strategy is also critical: higher frequencies (L. Manunza et al. 2025) and sight lines that avoid small impact parameters R (e.g., scheduling away from superior conjunction) help mitigate broadening, while at sub-GHz frequencies, width-aware detection should be the default rather than assuming δ-like signals. Recasting nondetections with width-aware pipelines will clarify how much of the Great Silence reflects a true absence of transmitters versus selection effects. Looking ahead, low-frequency facilities (e.g., SKA-Low) and modern wide-field arrays should incorporate these considerations into both design and pipelines to ensure that broadened technosignatures are not systematically missed.

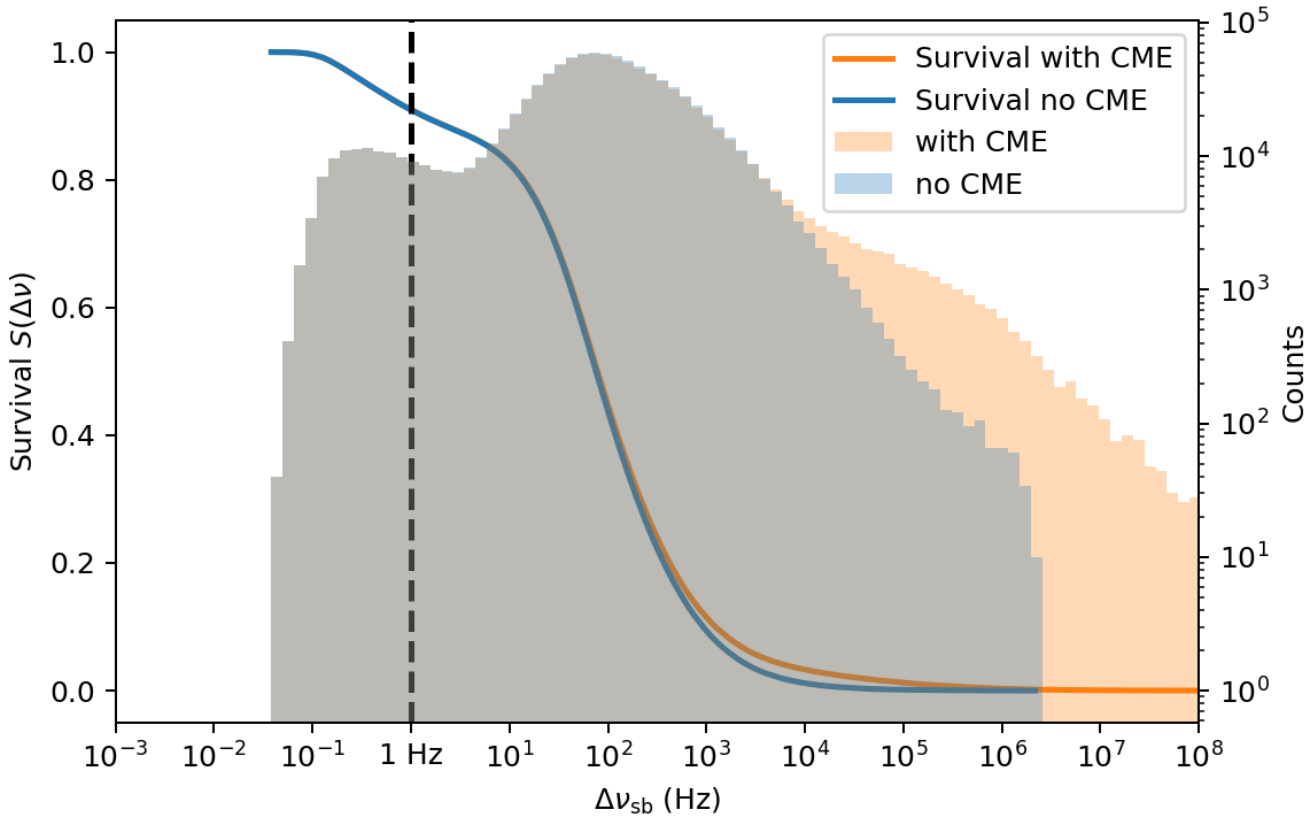

Figure 11. Similar to Figure 10, but for an observing frequency of 100 MHz. More than 90% of systems experience some degree of spectral broadening, with approximately 60% exhibiting $\geqslant$100 Hz of broadening, significantly degrading the detected transmitted power. Future radio technosignature searches with sensitive facilities such as SKA−Low should account for these constraints when designing search pipelines.

8. Conclusion

We report one of the first quantitative frameworks for assessing the impact of stellar environments—particularly turbulence (Section 5.2) and transient activity such as CMEs (Section 3)—on the detectability of narrowband technosignatures. Using a combination of first-principles models (Section 2) and empirical constraints (Section 4), we show that Doppler-induced spectral broadening caused by plasma irregularities in the Exo-IPM can significantly distort narrowband signals during their propagation from an ETI transmitter toward Earth. In Section 3, we present one of the first detailed treatments of CME properties that influence spectral broadening, including their speeds (Section 3.1) and turbulence strengths (Section 3.2). In Section 3.3, we further show how anisotropies introduced by CMEs can amplify spectral broadening by several orders of magnitude. In Section 4, we validate our model by comparing it with perhaps the largest available samples of spectral broadening observed in spacecraft carrier signals within our own solar system and find excellent agreement in radial dependence across 1–200 stellar radii from all previous studies. In Section 5, we extended this model to dM environments, using updated turbulence scaling informed by recent wind and turbulence models. We show that the broadening can exceed 10–100 Hz for most systems. These levels of spectral broadening are large enough to shift otherwise detectable technosignatures below the sensitivity thresholds of current search pipelines optimized for sub-Hz channels. To quantify the true impact of the Exo-IPM, we perform Monte Carlo simulations (Section 6.3) over orbital configurations, turbulence environments, stellar types, and CME parameters. We derive survival functions for spectral broadening and show that more than >30% of systems at 1 GHz and >80% at 100 MHz exhibit broadening above 10 Hz. We also found that, although the probability of encountering a CME during a typical technosignature observation is low (<3%), in nearly all such cases, CMEs induce additional spectral broadening by several orders of magnitude. These results suggest that turbulence-induced spectral broadening—particularly in the dynamic environments of dMs—may offer a compelling explanation for the apparent absence of detected narrowband radio technosignatures. We recommend width-aware search strategies for future technosignature surveys to account for Exo-IPM-induced signal broadening effects.

Acknowledgments

V.G. and G.B. gratefully acknowledge support from the SETI Institute through the STRIDE grant (24STRIDE-005), which made this work possible. V.G. also thanks Andrew Siemion, Daniel Price, Ravi Kopparapu, and Brian Lacki for valuable discussions and insights that greatly contributed to shaping this study.

Appendix
Derivation of the Radial Dependence of the Scattering Measure

In this appendix, we outline a solution to the following integral from Equation (9) also given as,

$$\int_0^D C_{n_e}^2 \, dz \propto \int_0^D (R^2 + z^2)^{-p} \, dz. \tag{A1}$$

It should be noted that taking the upper limit $D \to \infty$ greatly simplifies the integral to a closed-form expression in terms of Gamma functions. This is justified when the integrand decays rapidly with z, so that most of the contribution to the scattering measure comes from regions near the star (i.e., where $R^2 + z^2 \approx R^2$). Thus, for analytical convenience, and noting that the integrand decays rapidly for steep power laws, we replace the finite upper limit D with infinity:

$$\int_0^D (R^2 + z^2)^{-p}\, dz \approx \int_0^\infty (R^2 + z^2)^{-p}\, dz.$$

To evaluate the integral, substitute $z = R\tan\theta$ so that $dz = R\sec^2\theta\, d\theta$ and $R^2 + z^2 = R^2\sec^2\theta$. Then,

$$\begin{aligned}\int_0^\infty (R^2 + z^2)^{-p}\, dz &= \int_0^{\pi/2} (R^2\sec^2\theta)^{-p}\ (R\sec^2\theta\, d\theta) \\ &= R^{1-2p}\int_0^{\pi/2} \sec^{2(1-p)}\theta\, d\theta \\ &= R^{1-2p}\int_0^{\pi/2} \cos^{2p-2}\theta\, d\theta.\end{aligned}$$

Using the standard result

$$\int_0^{\pi/2} \cos^{\mu}\theta\, d\theta = \frac{\sqrt{\pi}\,\Gamma\left(\frac{\mu+1}{2}\right)}{2\,\Gamma\left(\frac{\mu}{2}+1\right)},$$

with $\mu = 2p - 2$, we obtain

$$\int_0^{\pi/2} \cos^{2p-2}\theta\, d\theta = \frac{\sqrt{\pi}\,\Gamma\left(p-\frac{1}{2}\right)}{2\,\Gamma(p)}.$$

Thus, the evaluated integral is

$$\int_0^\infty (R^2 + z^2)^{-p}\, dz \propto R^{1-2p}\,\frac{\sqrt{\pi}\,\Gamma\left(p-\frac{1}{2}\right)}{2\,\Gamma(p)}.$$

Thus, we can define the integral as

$$\int_0^D C_{n_e}^2\, dz \propto \int_0^D (R^2 + z^2)^{-p} \propto R^{1-2p}\,\frac{\sqrt{\pi}\,\Gamma\left(p-\frac{1}{2}\right)}{2\,\Gamma(p)}. \tag{A2}$$

ORCID iDs

Vishal Gajjar https://orcid.org/0000-0002-8604-106X
Grayce C. Brown https://orcid.org/0000-0002-0069-2778

References

Alvarado-Gómez, J. D., Drake, J. J., Cohen, O., Moschou, S. P., & Garraffo, C. 2018, ApJ, 862, 93
Argiroffi, C., Reale, F., Drake, J. J., et al. 2019, NatAs, 3, 742
Armstrong, J. W., Rickett, B. J., & Spangler, S. R. 1995, ApJ, 443, 209
Azzollini, F., Emslie, A. G., Clarkson, D. L., Chrysaphi, N., & Kontar, E. P. 2024, ApJ, 968, 72
Bandyopadhyay, R., Beattie, J. R., & Bhattacharjee, A. 2025, ApJL, 982, L45
Bird, M. K., Paetzold, M., Edenhofer, P., Asmar, S. W., & McElrath, T. P. 1996, A&A, 316, 441
Bloot, S., Vedantham, H. K., Kavanagh, R. D., Callingham, J. R., & Pope, B. J. S. 2025, A&A, 695, A176
Bradford, H. M., & Routledge, D. 1980, MNRAS, 190, 73P
Brin, G. D. 1983, QJRAS, 24, 283
Brzycki, B., Siemion, A. P. V., de Pater, I., et al. 2023, ApJ, 952, 46
Brzycki, B., Siemion, A. P. V., de Pater, I., et al. 2024, AJ, 168, 284
Čalogović, J., Dumbović, M., Martinić, K., Temmer, M., & Vršnak, B. 2025, A&A, 695, A64
Choza, C., Bautista, D., Croft, S., et al. 2024, AJ, 167, 10
Cocconi, G., & Morrison, P. 1959, Natur, 184, 844
Cordes, J. M., & Lazio, T. J. 1991, ApJ, 376, 123
Crosley, M. K., & Osten, R. A. 2018, ApJ, 862, 113
Crowley, J., Wheatland, M. S., & Yang, K. 2024, MNRAS, 530, 457
Dewey, R. M., Baker, D. N., Anderson, B. J., et al. 2015, JGRA, 120, 5667
Efimov, A. I., Lukanina, L. A., Rudash, V. K., et al. 2013, CosRe, 51, 13
Efimov, A. I., Samoznaev, L. N., Andreev, V. E., et al. 2002, AdSpR, 30, 453
Efimov, A. I., Samoznaev, L. N., Bird, M. K., Chashei, I. V., & Plettemeier, D. 2008, AdSpR, 42, 117
Engle, S. G. 2024, ApJ, 960, 62
Enriquez, J. E., Siemion, A., Foster, G., et al. 2017, ApJ, 849, 104
Fainberg, J., & Stone, R. G. 1971, SoPh, 17, 392
Fallows, R. A., Iwai, K., Jackson, B. V., et al. 2023, AdSpR, 72, 5311
Gajjar, V., Perez, K. I., Siemion, A. P. V., et al. 2021, AJ, 162, 33
Goldstein, R. M. 1969, Sci, 166, 598
Goldstein, R. M., Bathker, D. A., Brown, D. W., et al. 1967, The Superior Conjunction of Mariner IV No JPL–TR-32-1092, NASA https://ntrs.nasa.gov/citations/19670016669
Good, S. W., Rantala, O. K., Jylhä, A. S. M., et al. 2023, ApJL, 956, L30
Gopalswamy, N., Lara, A., Lepping, R. P., et al. 2000, GeoRL, 27, 145
Güdel, M. 2002, ARA&A, 40, 217
Guhathakurta, M., Holzer, T. E., & MacQueen, R. M. 1996, ApJ, 458, 817
Hamilton, K., Smith, C. W., Vasquez, B. J., & Leamon, R. J. 2008, JGRA, 113, A01106
Heath, M. J., Doyle, L. R., Joshi, M. M., & Haberle, R. M. 1999, OLEB, 29, 405
Henry, T. J., & Jao, W.-C. 2024, ARA&A, 62, 593
Johnson, O. A., Gajjar, V., Keane, E. F., et al. 2023, AJ, 166, 193
Kontar, E. P., Chen, X., Chrysaphi, N., et al. 2019, ApJ, 884, 122
Korpela, E. J., Anderson, D. P., Cobb, J., et al. 2025, AJ, 170, 112
Krieger, A. S., Timothy, A. F., & Roelof, E. C. 1973, SoPh, 29, 505
Leblanc, Y., Dulk, G. A., & Bougeret, J.-L. 1998, SoPh, 183, 165
Leitzinger, M., Odert, P., & Greimel, R. 2024, MNRAS, 532, 1486
Lingam, M., & Loeb, A. 2017, ApJ, 848, 41
Manoharan, P. K. 2006, SoPh, 235, 345
Manoharan, P. K. 2010, SoPh, 265, 137
Manunza, L., Vendrame, A., Pizzuto, L., et al. 2025, AcAau, 233, 155
Margot, J.-L., Greenberg, A. H., Pinchuk, P., et al. 2018, AJ, 155, 209
Margot, J.-L., Li, M. G., Pinchuk, P., et al. 2023, AJ, 166, 206
Mesquita, A. L., & Vidotto, A. A. 2020, MNRAS, 494, 1297
Morabito, D. D., Shambayati, S., Finley, S., & Fort, D. 2003, ITAP, 51, 201
Morin, J., Donati, J.-F., Petit, P., et al. 2010, MNRAS, 407, 2269
Munro, R. H., & Jackson, B. V. 1977, ApJ, 213, 874
Newkirk, G., Jr. 1967, ARA&A, 5, 213
Ng, C., Rizk, L., Mannion, C., & Keane, E. F. 2022, AJ, 164, 205
Odert, P., Leitzinger, M., Hanslmeier, A., & Lammer, H. 2017, MNRAS, 472, 876
Painter, C., Croft, S., Lebofsky, M., et al. 2025, AJ, 169, 222
Parker, E. N. 1958, ApJ, 128, 664
Pizzolato, N., Maggio, A., Micela, G., Sciortino, S., & Ventura, P. 2003, A&A, 397, 147
Price, D. C., Enriquez, J. E., Brzycki, B., et al. 2020, AJ, 159, 86
Qian, L. 2018, in 42nd COSPAR Scientific Assembly, F3.8–1–18
Reiners, A., Basri, G., & Browning, M. 2009, ApJ, 692, 538
Réville, V., Jasinski, J. M., Velli, M., et al. 2024, ApJ, 976, 65
Rickett, B. J. 1990, ARA&A, 28, 561
Robinson, P. A. 1992, SoPh, 137, 307
Rodriguez, L., Shukhobodskaia, D., Niemela, A., et al. 2024, A&A, 689, A187
Saito, K., Poland, A. I., & Munro, R. H. 1977, SoPh, 55, 121
Sakaue, T., & Shibata, K. 2021a, ApJ, 919, 29
Sakaue, T., & Shibata, K. 2021b, ApJL, 906, L13
Sasikumar Raja, K., Ingale, M., Ramesh, R., et al. 2016, JGRA, 121, 11,605
Shaikh, Z. I. 2024, MNRAS, 530, 3005
Siemion, A. P. V., Benford, J., Cheng-Jin, J., et al. 2014, Proc. Advancing Astrophysics with the Square Kilometre Array (Trieste: SISSA), 1
Siemion, A. P. V., Demorest, P., Korpela, E., et al. 2013, ApJ, 767, 94
Song, G.-Y., Tao, Z.-Z., Huang, B.-L., et al. 2025, arXiv:2509.06310
Sorriso-Valvo, L., Yordanova, E., Dimmock, A. P., & Telloni, D. 2021, ApJL, 919, L30
Spangler, S. R., Kavars, D. W., Kortenkamp, P. S., et al. 2002, A&A, 384, 654
Spangler, S. R., & Sakurai, T. 1995, ApJ, 445, 999
Stelzer, B., Marino, A., Micela, G., López-Santiago, J., & Liefke, C. 2013, MNRAS, 431, 2063
Tarter, J. 2001, ARA&A, 39, 511

Tarter, J. C., Backus, P. R., Mancinelli, R. L., et al. 2007, AsBio, 7, 30
Tasnim, S., Zank, G. P., Cairns, I. H., & Adhikari, L. 2022, ApJ, 928, 125
Tingay, S. J., Tremblay, C., Walsh, A., & Urquhart, R. 2016, ApJL, 827, L22
Tokumaru, M., Kojima, M., Ishida, Y., Yokobe, A., & Ohmi, T. 2000, AdSpR, 25, 1943
Veronig, A. M., Odert, P., Leitzinger, M., et al. 2021, NatAs, 5, 697
Vida, K., Leitzinger, M., Kriskovics, L., et al. 2019, A&A, 623, A49
Vidotto, A. A., Jardine, M., Morin, J., et al. 2013, MNRAS, 438, 1162
Vidotto, A. A., Jardine, M., Opher, M., Donati, J. F., & Gombosi, T. I. 2011, MNRAS, 412, 351
Vršnak, B., & Gopalswamy, N. 2002, JGRA, 107, 1019
Vršnak, B., Ruždjak, D., Sudar, D., & Gopalswamy, N. 2004, A&A, 423, 717
Vršnak, B., & Žic, T. 2007, A&A, 472, 937
Wang, J., Xin, L. P., Li, H. L., et al. 2021, ApJ, 916, 92
Webb, D. F., & Howard, T. A. 2012, LRSP, 9, 3
Wheatland, M. S. 2003, SoPh, 214, 361
Woo, R. 1978, ApJ, 219, 727
Woo, R. 2007, SpWea, 5, 09004
Woo, R., & Armstrong, J. W. 1979, JGR, 84, 7288
Woo, R., Yang, F. C., & Ishimaru, A. 1976, ApJ, 210, 593
Wood, B. E., Linsky, J. L., Müller, H.-R., & Zank, G. P. 2001, ApJL, 547, L49
Wood, B. E., Müller, H.-R., Redfield, S., et al. 2021, ApJ, 915, 37
Xie, H., Ofman, L., & Lawrence, G. 2004, JGRA, 109, A03109
Yakovlev, O. I., Efimov, A. I., Razmanov, V. M., & Shtrykov, V. K. 1980, SvA, 24, 454
Yashiro, S., Gopalswamy, N., Michalek, G., et al. 2004, JGRA, 109, A07105